U.PORTO
FACULDADE DE CIÊNCIAS
UNIVERSIDADE DO PORTO

MSc

MSc

2.º
CICLO

FCUP
2019

U.PORTO

Detecting the atmosphere of exoplanets using
high resolution spectroscopy

Eduardo Alexandre de Sousa Cristo

FC

U.PORTO
FACULDADE DE CIÊNCIAS
UNIVERSIDADE DO PORTO

Detecting the atmosphere of exoplanets using high resolution spectroscopy

MSc

MSc

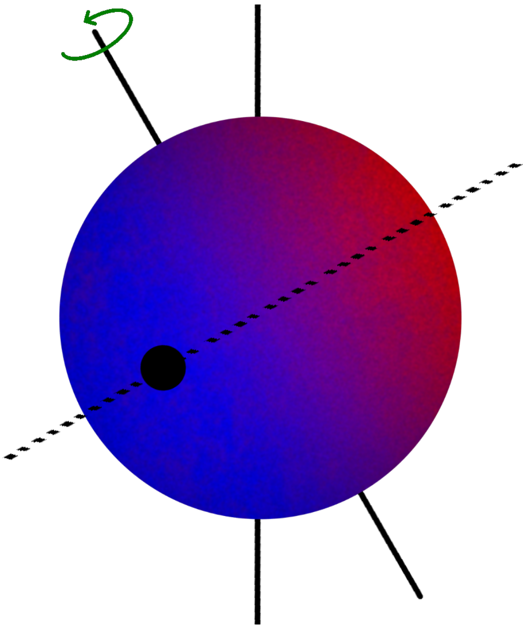

Detecting the atmosphere of exoplanets using high resolution spectroscopy

Eduardo Alexandre de Sousa Cristo
Mestrado em Astronomia e Astrofísica
Departamento de Física e Astronomia
2019

Orientador
Nuno Cardoso Santos, Professor, Departamento de Física e Astronomia, FCUP e
Investigador, Instituto de Astrofísica e Ciências do Espaço

U.PORTO

FC FACULDADE DE CIÊNCIAS
UNIVERSIDADE DO PORTO

Todas as correções determinadas pelo júri, e só essas, foram efetuadas.

O Presidente do Júri,

Porto, ______/______/_________

MSc

Resumo

As ciências planetárias são um ramo da astrofísica que se têm desenvolvido rapidamente nas últimas décadas. Missões robóticas visitaram todos os planetas do sistema solar, a maioria das luas e alguns dos corpos sub-planetários. A quantidade de dados existentes para os caracterizar é de especial importância se quisermos inferir as propriedades de outros sistemas planetários que, até este momento, não nos são possíveis de alcançar. Quando comparados com os corpos do nosso sistema planetário, o desenvolvimento de novas ferramentas para identificar a pluralidade dos mundos está a acontecer a um ritmo acelerado. Esta tarefa não se têm revelado fácil! Existem limitações observacionais, os melhores dos nossos telecópios estão limitados a observações a partir do solo e os recursos no espaço são limitados e caros. Em particular a deteção e caracterização das atmosferas dos exoplanetas requer espectroscopia de alta resolução e um sinal suficientemente bem definido para se distinguir do ruído. Tendo estes fatores em conta, é desenvolvida aqui uma nova técnica que permite, utilizando todos os dados já disponíveis, agregar observações e concluir se existe atmosfera no planeta. Partindo de um conjunto de pressupostos e dados de qualidade suficiente é possível deduzir os perfis de temperatura, pressão e densidade. Neste trabalho são descritos os princípios do algorítmo que, sabendo um determinado número de parâmetros estelares e planetários, é usado para obter quantidades físicas características das atmosferas dos exoplanetas.

Abstract

The planetary science as an astrophysics branch has been in a fair development in the last decades. Unmanned missions have visited all the planets of the solar system, most of the moons and some of the minor planetary bodies. The amount of data we have to characterize them is of the foremost importance if we want to infer about the properties of planetary systems, at this moment, out of our reach. In comparison with the bodies of our planetary system, the development of new techniques to identify the vast plurality of worlds arise at a fast pace. But this is no easy task! We are limited by observational constrains, the best of our telescopes are limited to ground observations and the resources at space are limited and expensive. In particular, the detection and characterization of exoplanets atmospheres require high precision spectroscopy and reasonably high signal-to-noise ratios. With this in mind, it is developed here a new technique that allows, recurring to all the data available, combining observations and deduce if a planet has atmosphere. Departing from a set of assumptions and with data of enough quality, it is possible to deduce the temperature profiles, pressure or density. It is described in this work a routine that is self contained and, known the sufficient number of planetary and stellar parameters, used to obtain the relevant quantities characteristic of the exoplanets atmospheres.

Acknowledgements

I must confess that any recognition that I'll make here is shallow compared with the amount of effort and hours of work that people who helped me dedicated. Foremost I'll like to demonstrate my special gratitude to Dr. Nuno C. Santos. He was the person I always wanted to work with and I was really happy with his acceptance to be my advisor. His positiveness, experience and recognized scientific work was an inspiration and at the same time, for me, a responsibility to don't let anyone down. I would like also to demonstrate my appreciation to the exoplanets team, whose work is undoubtfully the best we have in Portugal. I owe a special gratitude to Dr. Olivier D. S. Demangeon, who helped me in the technical questions along the way, and Dr. Jorge H. C. Martins that supported me when I needed. Inserted in the CAUP activities the Journal Club on exoplanets was, every time, a joy to participate with insightful papers and discussions.

At last but not least I've to be grateful to my parents, sister and closer family who where always there, for the best and for the worst. To the friends I made along this path, some of which share the same passion for Astronomy. In a broader sense to the CAUP/IA institution that helps to project the work it is done, but remembering that nothing of this would be possible without the great and driven people who works on it.

Contents

List of Figures

List of Tables

Chapter 1.
Introduction

1.1 Historical background

Since the dawn of humanity Astronomy has been a fundamental tool. It took an important role when the first humans became sedentary. The success of a given crop was highly dependent on seeding epoch, so it became necessary a way to measure time. A proof of it can be found in Stonehenge: at the first day of the summer solstice, the sun aligns in such a way its brightness can be seen through the openings of the standing stones.

The systematization of Astronomy as a modern science only came when Humans started to colonize new territory on Earth. Exploring uncharted places, it was necessary to develop a new method to derive latitude and longitude. Tools like the Astrolabe and Quadrant were used to measure the relative position of celestial bodies in the sky. By comparison it was then possible to have an estimate of the relative position on the surface of the Earth. Most of this concepts were refined and developed up to the modern era. The precise measurement of time was replaced by more accurate methods, like the measurement of oscillations of Cesium in an atomic clock. The position on the surface of the earth is now possible with unprecedented precision, result of the GPS satellites. The navigation with star positioning is still used in state of the art space probes, and it is a fundamental concept for space exploration of the Solar System.

The same force that made us explore Earth and discover new places is now on the rise in the Space Era. In the forthcoming decades there are plans to build moon bases and settle on Mars. In a few centuries it can even be possible to make Mars more similar to Earth. In a distant future the Solar System will be small and the desire expansion will thrive again.

What about other stars, are there planets outside our neighborhood? This question was unanswered and theme of debate since the ancient Greeks up to the end of the XX century. The formation of the solar system has been debated at least for as long, with various concurring hypothesis. The work of Immanuel Kant in his *Allgemeine Naturgeschichte und Theorie des Himmels* suggested a modified nebular hypothesis in which planets were originated in a disk as result of processes of accretion. In 1984 it was imaged the first protoplanetary disk around the star β-Pictoris, after a detection on the Infrared in the previous year (A. Smith and J. Terrile, 1985). Later, in 1992, the first planetary mass objects orbiting another star were found orbiting around a Pulsar in Virgo constellation (Wolszczan and Frail, 1992).

In 1995 the first exoplanet around a main-sequence was identified (Mayor and Queloz, 1995). With it a new class of exoplanets was brought to existence: Hot Jupiters. They are planets with at least 10% of Jupiter's mass, orbiting stars in a short period and at a short distance ($< 0.1 A.U.$). The finding was made using the Radial- velocities technique, chapter 1.3.1. Five years later it was observed the first planet transiting a star (Charbonneau et al., 2000). Subsequent studies allowed, using other methods (chapter 2), the development of tools to characterize exoplanetary atmospheres (Burrows, 2014).

In the present thesis we explore a new method to detect and characterize exoplanet atmospheres using high resolution spectroscopy and the Rossiter McLaughlin effect. To put it in context, we will start by presenting the basic principles of spectroscopy and photometry followed by a characteristics summary of the of the $HARPS$ spectrograph. It will be discussed the principles of detection of exoplanets, with particular focus on radial velocities. The different methods which form the basis of exoplanets atmospheres characterization are reviewed to introduce the method to be explored on chapter 4; finishing with the most relevant results and conclusions. The RM effect is explored in different wavelengths, fitting the radial velocity curves. The radius variation of the analyzed planet is recovered, as a atmospheric opacity measurement at different wavelength bins. The chromatic approach allows to infer about mostly the transmitted light in the atmosphere at visible wavelengths, dominated by Rayleigh scattering, section 1.4.1.

1.2 Principles of spectroscopy and photometry

1.2.1 Photometry

Photometry is the science which aggregates the techniques that allows us to measure precisely the flux of a source and infer its properties as result. The total energy output (luminosity), temperature and object size are some of the quantities and properties that can be obtained. Frequently in the visible portion of the spectra, the fluxes are measured using magnitudes. For two stars with flux F_1 and F_2, the magnitude difference can be computed by:

$$m_1 - m_2 = -2.5log\left(\frac{F_1}{F_2}\right), \tag{1.1}$$

where m_1, m_2 are magnitudes measured in some electromagnetic frequency band. Stars radiate along all the electromagnetic spectra and can be characterized by their spectral energy distribution (SED). Bolometric quantities are obtained if the power is integrated over the range of frequencies or wavelengths. The observation on different regions of the electromagnetic spectra require different detectors and telescopes, both on ground and space. Ground observations are limited by atmospheric visibility, which is opaque to X and γ radiation, as well as some IR bands due to the presence of water vapor.

A popular system of filters is the UBV, Fig.1.1, in the visible wavelength range. Measuring the magnitude of a star with two different bands, it is obtained the color of that star:

$$B_1 - B_2 = m_{B_1} - m_{B_2}, \tag{1.2}$$

where B_1 and B_2 are any two bands. This quantity gives the ratio between the integrated flux in two different regions of SED.

$$\frac{F_{B_1}}{F_{B_2}} = C10^{\frac{B_2-B_1}{2.5}}, \tag{1.3}$$

with C fixing the zero of the scale. By definition, the reference star Vega was set to have

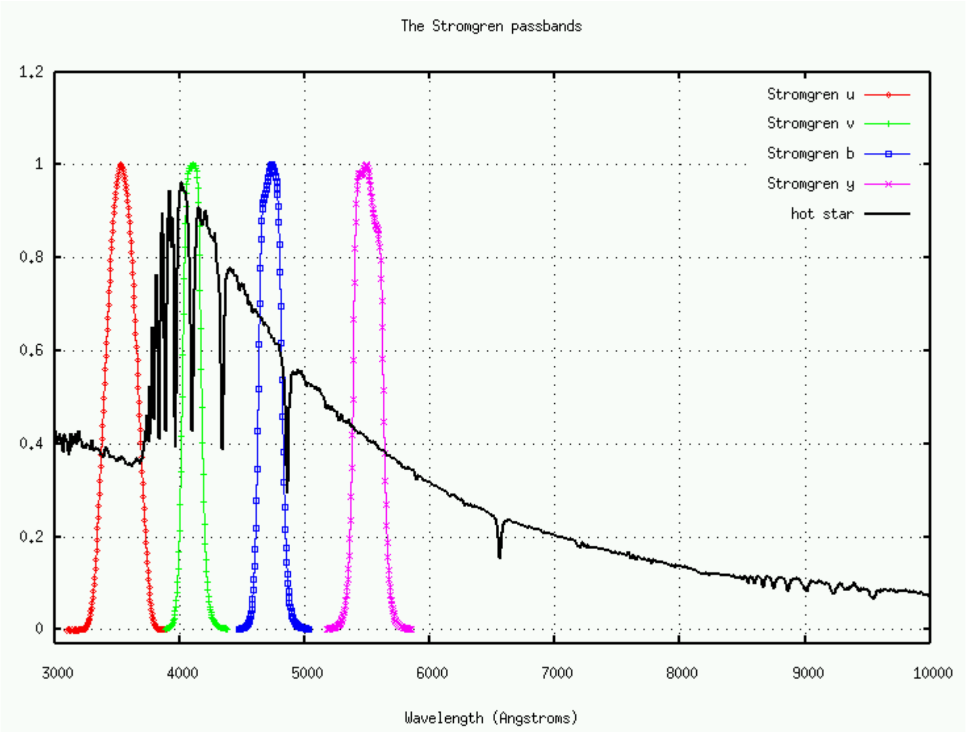

Figure 1.1: Stromgren UVBY filter transmission curves superimposed to a hot star SED. This set in particular has the advantage to be useful to measure the interstellar extinction.Copyright: Michael Richmond

$(B-V)=0$. A star with an higher effective temperature will have a negative $(B-V)$ color, and a cooler a positive value. High precision photometry is crucial to measure low magnitude variations with time, like in the case of planets transiting their host star, chapter 2. The reduction of photometric noise can be achieved by differential photometry, comparing the magnitude of the target star to a reference one, equation (1.2). With CCDs the noise can be further reduced. Simultaneously the flux of the background in the field can be compared with multiple stars. Since they are measured with the same instruments, offsets can be avoided. This method is able to achieve a precision $\lesssim 1mmag$

1.2.2 Spectroscopy

The basic spectrograph is composed of a slit, fixed or variable in width, in order to select the objects in the focal plane; a colimator to turn the diverging light rays into parallel ones; a diperser and a detector. For a photon of wavelength λ, the angle of dispersion for the order of dispersion maxima m, θ_m, at a θ_i angle of incidence on the plane is described by the grating equation:

$$\theta_m = arscsin\Big(sin(\theta_i) - \frac{m\lambda}{d}\Big), \tag{1.4}$$

where d is the distance between the rulings in the dispersion grating. The dependence of the dispersion of the orders with the wavelength is found by differentiating (1.4) in order to the wavelength.

$$\frac{d\theta_m}{d\lambda} = \frac{m}{dcos(\theta_m)}. \tag{1.5}$$

When in a Littrow configuration the angle of incidence is equal to the angle of dispersion:

$$\frac{d\theta_m}{d\lambda} = \frac{2tan(\theta_m)}{\lambda}. \tag{1.6}$$

In a conventional spectrograph low orders are used to avoid overlap of different wavelengths. Echelle spectrographs, with the slits in a "ladder" configuration (Fig.1.2.2), differently have $\theta_m \approx 2$, low spectral range,$\delta\lambda = \lambda_m - \lambda_{m-1}$, and as consequence high order of dispersion. To avoid the orders overlap are cross-dispersed introducing an échelle grating. The spectral resolution R is a measurement of the ratio between the wavelength range and the minimum distance of two well defined absorption lines. It can define the minimum distance from which two spectral lines can be resolved:

$$R = \frac{\lambda}{\Delta\lambda}. \tag{1.7}$$

The spectral range is inversely proportional to the order number. The angular spread, δ_m:

$$\delta_m = \frac{\lambda^2}{2dsin(\theta_m)}, \tag{1.8}$$

with each échelle order covering a different range interval of the spectra.

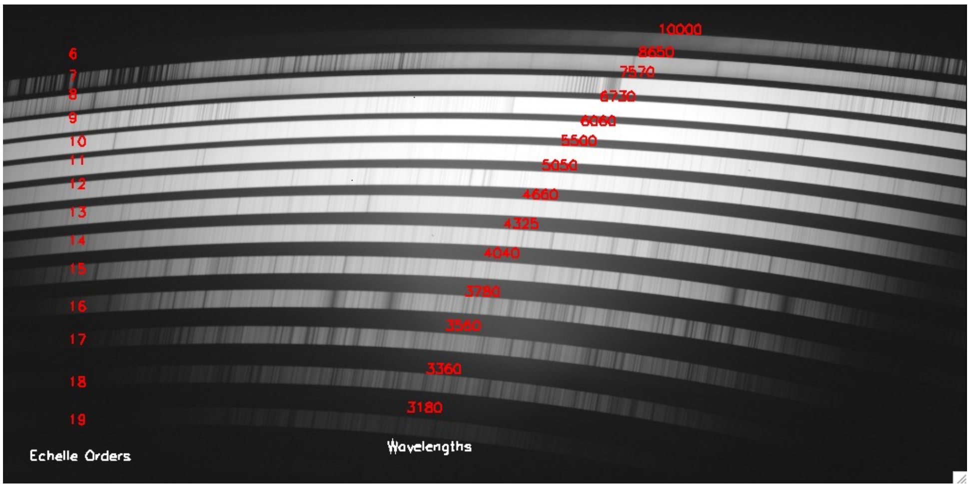

Figure 1.2: Solar spectra captured by the Magellan Echellette ($MagE$) spectrograph. It operates with slit width from 0.5 to 5.0 $arcsec$, and has a resolution of $R = 4100$ with the $1arcsec$ slit width. The order numbers and central wavelengths are indicated. Credits: Marshall et al. (2008).

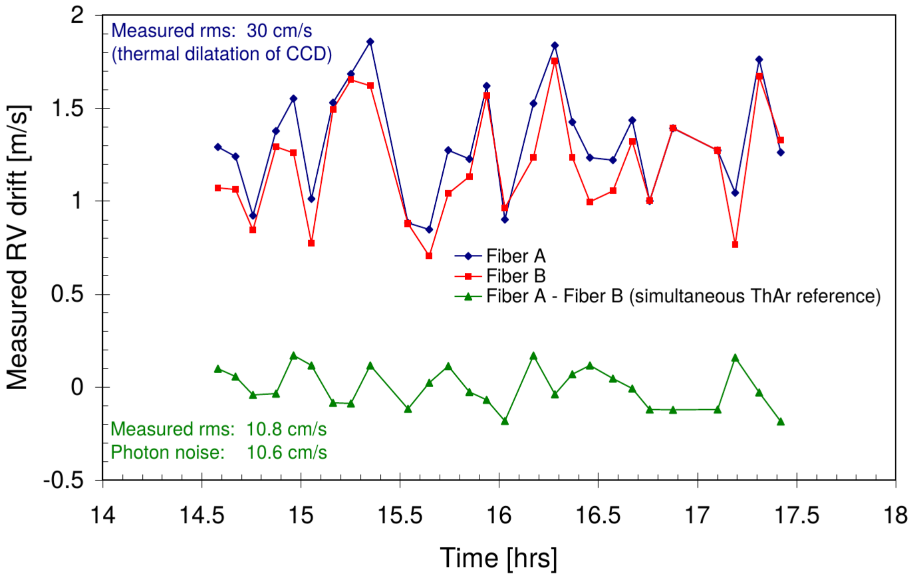

Figure 1.3: Radial velocity drift in a time span of 3 hours. The simultaneous calibration of fiber A and B, allows a radial velocity rms below $1m/s$. The main contribution for the noise at these levels is the thermal variations of the CCD sensor, contributing with $\sigma_{RV,Thermal} = 30cm/s$. Credits: Rupprecht et al. (2004)

HARPS Spectrograph

The High-Accuracy Radial Velocity Planetary Searcher, HARPS, is an échelle type fiber-fed spectrograph (Mayor et al., 2003). The light is injected through two fibers: one conducting the target light, and the other with a calibration source (lamp or reference star). The light is dispersed in 72 orders for each fiber, covering a wavelength range from $380nm$ to $690nm$. The fiber diameter, with an aperture of 1 $arcsec$ in the sky, defines a slit width that produces a resolution $R = 115000$. At the focal plane, one resolution element is sampled by 3.2 pixels. The calibration fiber is fed with a Th-Ar lamp or with a Fabry-Pérot, in a vacuum that guarantees drifts below $1m/s$ per day, Fig.1.3. The vessel that contains the spectrograph is maintained at a constant temperature of 17^oC, with a stability of the order 0.01^oC

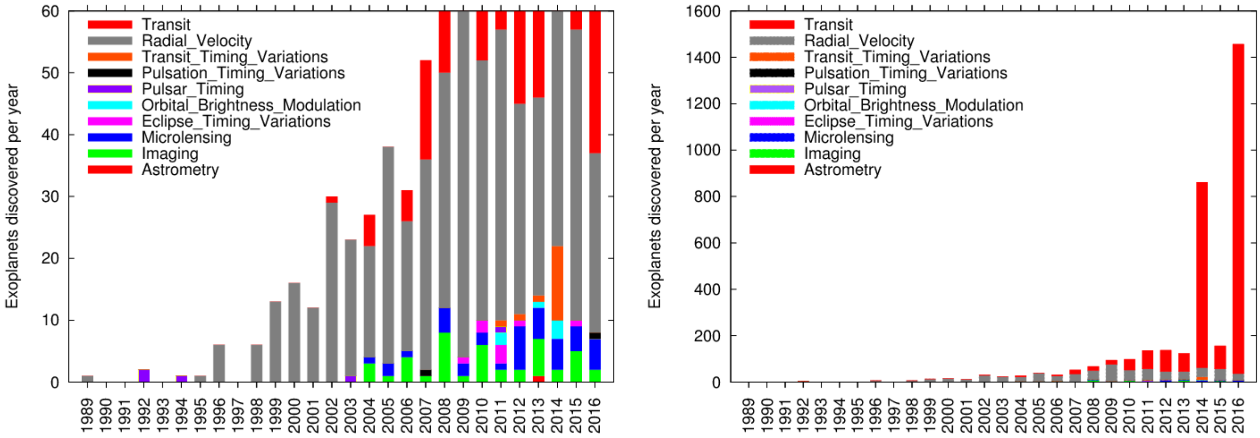

Figure 1.4: Comparison of the number of exoplanets discovered by year with different techniques. The 1989 detection is yet to be confirmed as the first one, the detected planet as a mass $\sim 11M_{Jupiter}$ and it is not ruled out as a brown dwarf. Copyright: Michael Richmond

1.3 Methods of detection and characterization of exoplanets

The number of exoplanets discovered since the detection of 51 Pegasi around a solar type star (Mayor and Queloz, 1995) has grown at a fast pace, mainly due to development of new techniques and more sensitive instruments, Fig.1.4. This section will focus in particular on two of them: radial velocities and transit photometry. In section 1.3.3 the basic principles of other techniques will be referred, with special importance on Direct Imaging. Finally it will be deduced the relation between the(Mayor and Queloz, 1995) radius of the planets and their host stars both in the visible and IR.

1.3.1 Radial velocities

The presence of a planet orbiting a star generating a perturbation in radial velocity is created by the movement of both bodies around the system center of mass (CM). The measurement is made measuring the Doppler effect on the host spectral lines. The Keplerian orbit of a body with semi-major axis , a, around the host star can be defined to have a semi-major axis a_1 around the CM:

$$a = \frac{M_P}{M_P + M_*} = \frac{M_P}{M}, \tag{1.9}$$

if M is the total mass of the system. The body has an elliptically shaped orbit around the CM, which can be expressed in polar coordinates (1.10).

$$r_1 = a_1 \frac{1-e^2}{1+ecos(f)}, \tag{1.10}$$

where e is the orbital eccentricity and f the true anomaly, defined as the angle formed by the periastron (closest approach point) and the orbital position from the center of mass reference point. In rectangular coordinates with the referential origin in the CM and the x-axis direction aligned with the periastron:

$$\bar{r_1} = \begin{bmatrix} r_1 cos(f) \\ r_1 sin(f) \end{bmatrix}, \tag{1.11}$$

$$\dot{\bar{r_1}} = \begin{bmatrix} \dot{r_1} cos(f) - r_1 \dot{f} sinf \\ r_1 \dot{f} cos(f) + \dot{r_1} sinf \end{bmatrix}. \tag{1.12}$$

From equation (1.10) in polar coordinates, it is possible to rewrite the $\dot{\bar{r_1}}$:

$$\dot{\bar{r_1}} = \frac{-h_1 sin(f)}{M_* a_1 (1-e^2)(cos(f)+e)}, \tag{1.13}$$

introducing h_1 as the angular momentum of the body M_*, which derivation follows from the universal gravitational law:

$$h_1 = \left(\frac{G M_*^2 M_P^4 a (1-e)^2}{M^3} \right)^{\frac{1}{2}}, \tag{1.14}$$

which plugged in into equation (1.13):

$$\dot{\bar{r_1}} = \frac{G M_P^2}{M a (1-e^2)} \begin{bmatrix} -sin(f) \\ cos(f)+e \end{bmatrix}. \tag{1.15}$$

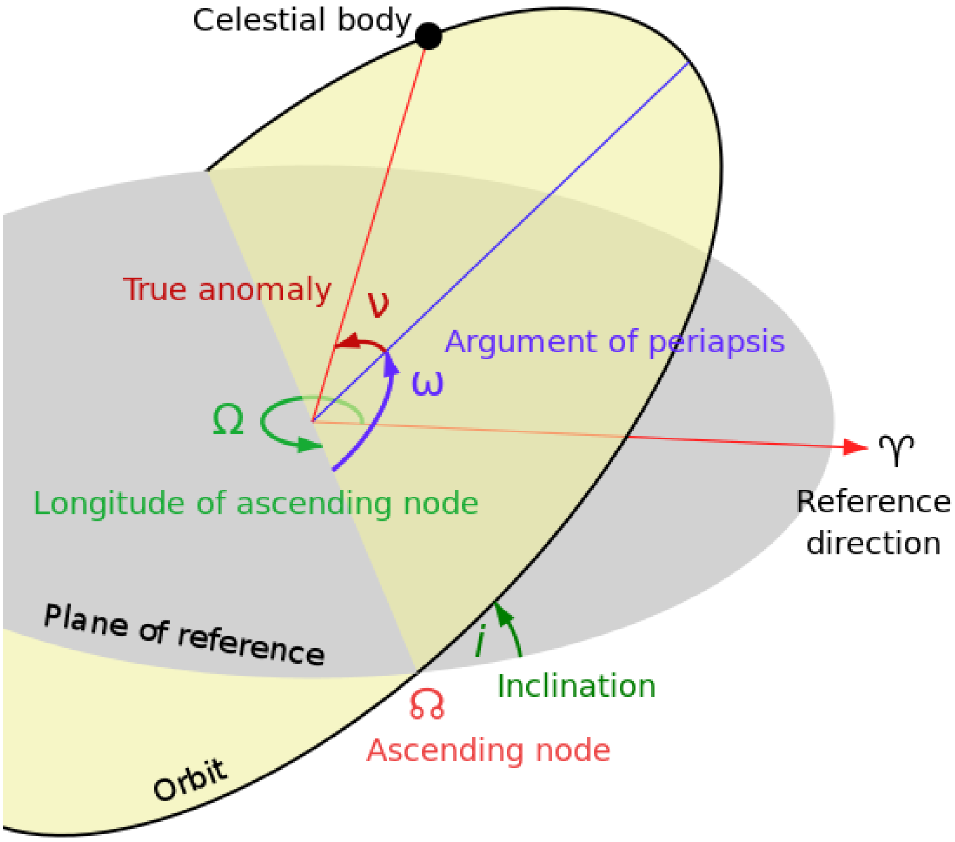

Figure 1.5: Diagram depicting the orbital plane characterized by quantities of the reference plane. From the observer point of reference γ, the celestial body describes an orbit with inclination measured from a reference plane. In the orbital plane, the argument of periapsis defines the between the line of nodes at the ascending node to the periapsis. The true anomaly gives the angle from ω to the current celestial body position. In the plane of reference, the angle between the reference direction and and the lines of the nodes is given by the longitude of the ascending node. By Lasunncty at the English Wikipedia, CC BY-SA 3.0, https://commons.wikimedia.org/w/index.php?curid=8971052

From an observational standing, the velocity vector is projected in the plane of the sky. To better understand the geometry of the problem Fig.1.5 expresses the main orbital quantities that describe the dynamics from an observer point of view. The vector of sight $\bar{k}$, can be defined in the three spatial directions by the following:

$$\bar{k} = \begin{bmatrix} sin(\omega)sin(i) \\ cos(\omega)sin(i) \\ cos(i) \end{bmatrix}. \tag{1.16}$$

The observed velocity results of the projection of $\dot{\bar{r_1}}$ into the observation vector $\bar{k}$, given by the dot product:

$$v = \dot{\bar{r_1}}.\bar{k} = \left(\frac{G}{Ma(1-e^2)}\right)^{\frac{1}{2}} M_P sin(i)(cos(\omega + f) + ecos(\omega)). \tag{1.17}$$

The radial velocity semi-amplitude K is found by halving the difference between the maximum and minimum values of v:

$$K = \frac{|v_{max} - v_{min}|}{2} = \left(\frac{G}{Ma(1-e^2)}\right)^{\frac{1}{2}} M_P sin(i), \tag{1.18}$$

where $M_P sin(i)$ corresponds to the planet minimum mass. From radial velocities it is possible to directly measure both the period T and K. The $M_P sin(i)$ is known if the stellar mass, when $M_* \gg M_P$, is found by alternate methods, like spectral synthesis and asteroseismology. It is worth to note that in general the inclination is not know with precision. This is not a major problem since the inclination distribution of orbital planes is statistically favorable to edge-on systems. If a Solar System analogue is observed in an edge-on configuration, the expected semi-amplitude $K^{\oplus} = 9.0 \times 10^{-2}\ m/s$ and for Jupiter-Sun $K^{♃} = 12.7\ m/s$. The detection of rocky planets down to the mass of the Earth require a radial velocity precision below $1m/s$.

The motion of the stars around the CM is measured by an observer as a change of a given spectral line peak wavelength with time. A photon of wavelength λ_0 emitted by a source moving with a velocity component along the line of sight vector will be detected with a new wavelength λ:

$$\lambda = \lambda_0 \frac{1 + \left(\frac{\bar{k}.\bar{v}}{c}\right)}{1 - \left(\frac{v}{c}\right)^2}, \tag{1.19}$$

where $\bar{v} = \dot{\bar{r_1}}$ defined in equation (1.12). In general relativity, the curvature of a region of the space-time is responsible to introduce a similar effect: the gravitational redshift. Assuming a system observed from a zero potential frame, the intensity distribution is approximated by Planck's law. In a stellar spectra, the shift in the photospheric absorption lines can be measured simultaneously using the cross correlation function, CCF, between it and a rest frame analogue, chapter 2. If the conditions of the problem are in the non-relativistic framework, which is valid for radial velocity precision $\gtrsim 0.1 m/s$; equation (1.20) can be simplified:

$$\frac{\bar{k}.\bar{v}}{c} = \frac{\lambda_B - \lambda_0}{\lambda_0}, \tag{1.21}$$

where λ_0 is the reference wavelength measured form the ICRS. The effective radial velocity magnitude is frequently not known due to perturbing effects (Fischer et al., 2016). Gravitational perturbations account for uncounted fields in the relativistic approach and stellar convective dynamics introduce non homogeneous radial velocity variations with time, to name two of those perturbations (Lindegren and Dravins, 2003).

Photon noise limit contribution

The RV measurements are limited by photon noise. Following the analysis developed by Connes (1985), spectra can be used to estimate the uncertainty in radial velocity in single pixels or in the entire spectra. Bouchy, Pepe, and Queloz (2001) summarize the basic principles of the spectral lines contribution for this error. A reference spectra A_0 at a reference radial velocity is considered noise free. It is characterized by an intensity $A_0(i)$ and correspondent wavelength $\lambda(i)$ at the pixel i. The observed spectra A is considered a transformed version of A_0 by Doppler shift. If no other sources of noise are considered, both have the same intensity level per pixel. For an high resolution spectra:

$$\frac{\partial A_0(i)}{\partial \lambda(i)} \approx \frac{A(i) - A_0(i)}{\delta \lambda(i)}. \tag{1.22}$$

---

[0] The observation stations are actually not in a rest frame. The International Astronomical Union (IAU) defined the International Reference System ($ICRS$) from which all the wavelengths are measured:

$$\lambda = \lambda_0 \frac{1 + \left(\frac{\bar{k}.v_{\bar{o}bs}}{c}\right)}{1 - \left(\frac{\Phi_{obs}}{c^2}\right) - \frac{1}{2}\left(\frac{v}{c}\right)^2}. \tag{1.20}$$

Taking the differential form of equation (1.21), where $\bar{k}.\bar{v} = V$:

$$\frac{\delta V}{c} = \frac{\delta \lambda}{\lambda}, \tag{1.23}$$

together with (1.22), it is found a relation between the measured velocity at pixel i comparing both spectra.

$$\frac{\delta V(i)}{c} = \frac{A(i) - A_0(i)}{\lambda(i)(\partial A_0(i)/\partial \lambda(i))}. \tag{1.24}$$

An optimum weight $W(i)$ can be constructed considering that the noise from A is photon noise, as result of detector induced noise σ_D:

$$W(i) = \frac{\lambda(i)^2(\partial A_0(i)/\partial \lambda(i))^2}{A_0(i) + \sigma_D^2}. \tag{1.25}$$

The contribution for the measured velocity of the full spectra is recovered summing over all pixels in range:

$$\frac{\delta V}{c} = \frac{\sum(A(i) - A_0(i))\sqrt{\frac{W(i)}{A_0(i)+\sigma_D^2}}}{\sum W(i)}. \tag{1.26}$$

The optimum weight is inversely proportional to the square of the error of the velocity dispersion at each pixel. The uncertainty in the velocity for the complete spectrum,white-light , δV_{RMS} is computed summing the inverse square root of the weights:

$$\frac{\delta V_{RMS}}{c} = \frac{1}{\sqrt{\sum W(i)}}. \tag{1.27}$$

The estimation of the error can be generalized for wavelength bins, particularly useful to a chromatic analysis. The average velocity error, $\overline{\delta V_{RMS}}$, is computed similarly to the total error, summing for each slice k of the spectra:

$$\overline{\delta V_{RMS}} = \frac{1}{\sqrt{\sum \frac{1}{\delta V_{RMS}(k)}}}. \tag{1.28}$$

1.3.2 Transit photometry

A transit occurs when, from an observer point of view, a planet traverses the disk of a star. It can be observed in the solar system when there are the right geometrical conditions between an interior planet relative to an exterior one. Transits of Mercury and Venus can be seen from Earth. If the observed planet and star are closely aligned, the observed flux of the host star decreases by a fraction that depends on the radius ratio (R_P,R_*) and orbital radius, r. In the approximation where $r \gg \max\{R_P,R_*\}$, the flux decreases by a quantity (Seager and Mallén-Ornelas, 2003):

$$\Delta F = \left(\frac{R_P}{R_*}\right)^2 \tag{1.29}$$

For a planet with $R_P \approx R_\oplus$ orbiting a star with $R_* \approx R_\odot$ the variation of flux is $\Delta F \approx 10^{-4}$.

The probability of a random planet to transit depends on the system components radius, semi-major axis a and orbital eccentricity:

$$P = \left(\frac{R_P + R_*}{a}\right)\left(\frac{1}{1-e^2}\right). \tag{1.30}$$

The transit method relies mostly on multi-targeted surveys to detect new planets. The ground observations are mostly limited by atmospheric instability, with a current detectability threshold of $\Delta F \approx 10^{-3}$ (Wheatley et al., 2018). With this range we are capable to detect gas giants and characterize them in association with spectroscopic techniques. The orbital surveys are mostly limited by the aperture of the instrument, in a compromise between number of stars observed and precision. The search for longer period planets requires the observation of a fixed area of the sky, making it more limited than ground based observations. Placed well above the atmosphere, it is capable of detecting planets with $\Delta F \lesssim 10^{-4}$ in the range of Earth-like planets, as it is the case of Kepler space telescope (Koch et al., 2010). The transit light curves are a source to infer about not only the radius ratio (1.29) but also the period.

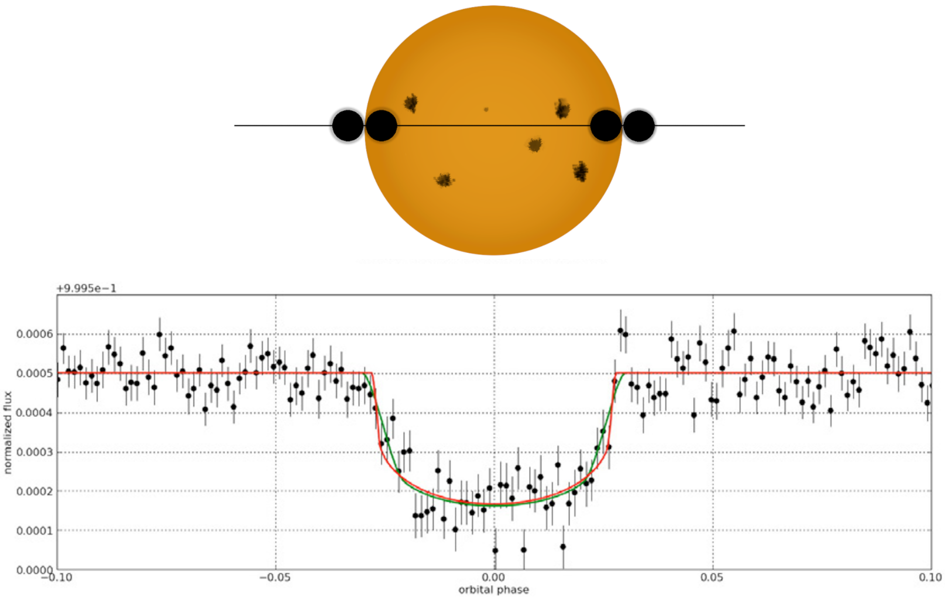

Figure 1.6: Variation of the observed flux of a star along the transit. At ingress and egress the shape of the light curve is defined by the amount of planetary area covering the stellar disk with time. Limb darkening of the stellar surface is responsible for the smoothing of the transition from the in transit to the out of transit light curve phase. Adapted from Leger et al. (2009), depicting the fit (black solid line) to the transit light curve of $CoRot - 7b$.

If the star radius is known , for $i = 90^{\odot}$ and $b = 0$; the transit time duration ΔT can be estimated by (1.31) (Seager and Mallén-Ornelas, 2003).

$$\Delta T = 13 \left(\frac{M_*}{M_\odot}\right) \left(\frac{R_*}{R_\odot}\right) \left(\frac{a}{1A.U.}\right)^{1/2} \tag{1.31}$$

1.3.3 Other methods

Astrometry

In comparison with radial velocities, that measure the motion of the star in the line of sight of an observer, the Astrometric method relies on the precise measurement of the position of a star hosting a planet, in the reference plane. The dynamical gravitational interaction between the masses of a Star-Planet system happens around their barycenter. Astrometry measures the associated motion projected in the sky plane:

$$\alpha = \frac{M_P}{M_* + M_P} a, \tag{1.32}$$

where M_* and M_P are the masses of the star and planet and a the semi-major axis of a simplified circular planetary orbit. The motion of the stars are often explored in the context of distance measurements using the parallax. The former equation can the be modified to express its angular nature using the Parsec definition,

$$\alpha = \left(\frac{M_P}{M_*}\right)\left(\frac{a}{1AU}\right)\left(\frac{1pc}{d}\right) arcsec, \tag{1.33}$$

in the approximation $M_* \gg M_P$. The distance to the star is given by d. From observation of equation (1.33), α increases with the distance to the star and it is larger to higher planet-star mass ratios and shorter distances. This technique is more sensitive to high mass planets with long orbital periods at nearby stars. For a Sun-Earth analogue at a distance of $10pc$ it is expected an astrometric signature $\alpha \approx 0.3\mu as$. Measurements below $1\mu as$ threshold are up to date challenging both from ground and space. There are several sources of noise. The atmospheric turbulence diffraction can, for example, introduce an uncertainty from $0.3 - 1$ arcsec, well above the threshold of most targets of interest (Perryman, 2011).

Timing

The dynamics of a system around a common center of mass can be measured from many ways. If the star of a system has periodic features in time, it is possible to infer the mass of the planet measuring time variations along an orbit as perturbations of the ideal orbit. Pulsars are among the ideal candidates to apply this technique. They are a class of neutron stars: the degenerate remains of a main-sequence star with a mass from $8M_\odot$ up to $20 - 25M_\odot$ (Kippenhahn and Weigert (1990)). The mechanisms and structure of the stars determine in part their final evolution. The final mass of a neutron star doesn't change very much, compared what it would be if it had a helium core. In a wide range of initial mass distributions, the presence of a CO core makes the output mass range be bounded to the interval of $[1, 3]M_\odot$. An intense magnetic field is capable of creating jets of particles from the poles by the syncrotron radiation mechanism. The period and axis of rotation determines if it can be detected and what is the frequency. The conservation of angular momentum guarantees the stability of the rotation period and, as consequence, of the measured signal.

A planet orbiting a pulsar creates a observed amplitude variation in the period described by equation (1.34) (Perryman (2011)):

$$\tau_p = \frac{asin(i)M_P}{cM_*}, \tag{1.34}$$

where i is the angle of projection in the line-of sight and c the velocity of light. Assuming a planet like the Earth in the best case scenario, orbiting at $1A.U.$ a pulsar with common mass of $M_* = 1.35M_\odot$ in line of sight at an angle $i = 90°$; it is measured $\tau_p \approx 1ms$. The precision and detection of the orbiting planet depends on the ratio between the times, and it is fundamentally limited by the Nyquist criterion. As τ_p is directly proportional to the orbiting mass, it is possible to detect lower mass bodies in the fastest pulsars.

Microlensing

Einstein's description of gravity predicted that a massive body should distort the space-time and as a consequence the light traveling nearby. The degree of curvature depends on the mass

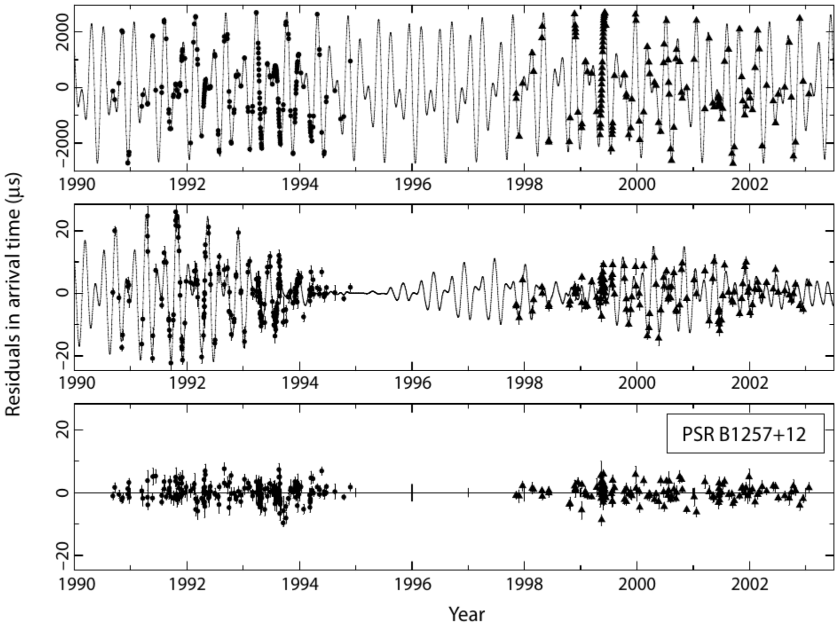

Figure 1.7: Daily-averaged arrival time residuals for PSR $B1257+12$ observed at 430 MHz with the Arecibo radio telescope. The top panel fits a model assuming the pulsar has no planetary companion. The middle panel uses a model using a 3 Keplerian fit assuming the same number of planetary mass objects.At the bottom it is presented the residuals after inclusion of the interactions between planets. Credits: Konacki and Wolszczan (2003)

of the body that acts as a lens. In the event of an alignment, the foreground object can be amplified and focused if the relative distance between the source, lens and observer is correct.

Microlensing is particular lensing phenomena where the source is not completely resolved. It is characterized by the mass of the lens, with masses typically stellar . As a star system crosses a distant source, the light is deflected by an angle α. If it is assumed circular symmetry the general relativity deflection is given by:

$$\alpha(r) = \frac{4GM(r)}{c^2 r} = \frac{2R_S(r)}{r}, \tag{1.35}$$

where $\alpha(r)$, $M(r)$ are the defection angle and mass up to the radius r and R_S Schwarzschild radius. This phenomena is dynamical in nature, the magnification and deflection is not constant with the time of observation or the angular distance. For a given lens, the planetary signature is seen as an increase in the observed flux. The star it orbits acts as a primary lens, and a second bump (Fig.1.8) indicates the presence of another mass that can be measured applying equation (1.35). Microlensing is highly sensitive to planets in Earth-to-Jupiter-like orbits with semi-major axes in the range 1–5AU (Beaulieu et al. (2006)).The use of this method is constrained by the unpredictability of lensing effects, as it can't be applied systematically in a field of the sky.

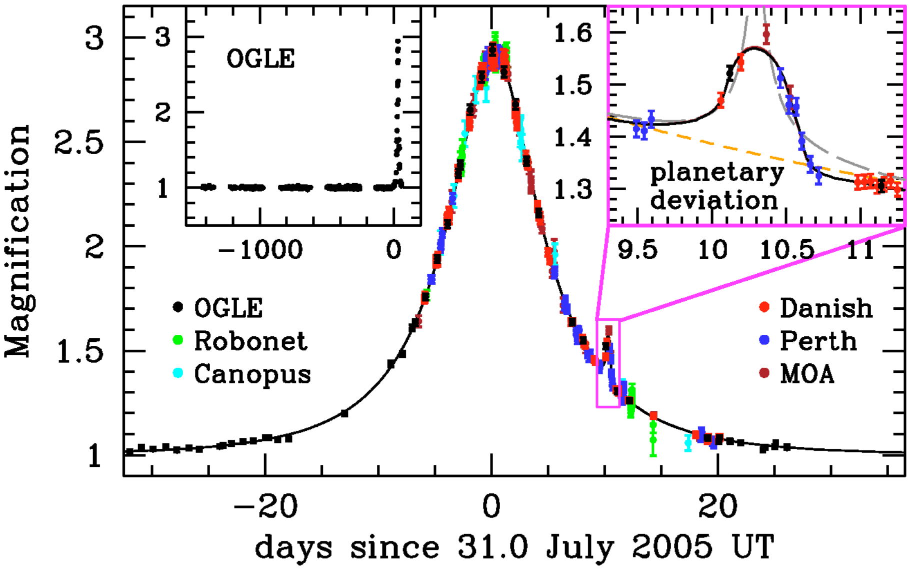

Figure 1.8: Observed light curve of the OGLE-2005-BLG-390 microlensing event and best fit model plotted as a function of time. The data set is composed of 650 data points from PLANET Danish (ESO La Silla, red points), PLANET Perth (blue), PLANET Canopus (Hobart, cyan), RoboNet Faulkes North (Hawaii, green), OGLE (Las Campanas, black), MOA (Mt John Observatory, brown). Credits: Beaulieu et al. (2006)

Direct imaging

Taking a direct image of an exoplanet relies on the techniques that both increase the contrast between the planet and star as well as measuring small angular regions. An exoplanet system is mostly dominated by the bolometric flux of the host star. Planets can have two major contributions for the observed flux: light produced by itself with origin in internal mechanisms and reflected radiation from the host star. At optical wavelengths, most of the light we see is stellar reflected light. At infra-red, however, it is possible to detect the emmited light from a planet. Assuming a black body approximation, a body at a temperature T has a spectral radiance distribution given by Planck's law (1.36). Following Seager, Dotson, and Institute (2010):

$$I_\lambda(T) = \frac{2hc^2}{\lambda^5(e^{\frac{hc}{\lambda k_B T}} - 1)}, \tag{1.36}$$

where h is Planck's constant. To estimate the contrast it is used the photon density per solid angle $\dot{n}(T)$, dividing equation (1.36) by the energy of a photon with frequency ν:

$$\dot{n}_\nu(T) = \frac{I_\nu(T)}{h\nu}; \dot{n}_\lambda(T) = \frac{I_\lambda(T)\lambda}{hc}. \tag{1.37}$$

If a star is at a distance d from an observer, it covers a projected solid angle in the sky:

$$\Omega = \pi\left(\frac{r}{d}\right)^2. \tag{1.38}$$

The flux of photons received, $\dot{N}$, can be obtained multiplying each of the equations on (1.37) by the solid angle:

$$\dot{N}_{\lambda,\nu} = \dot{n}_{\lambda,\nu}\Omega, \tag{1.39}$$

from where follows the contrast, C, as the ratio between the observed photon flux of the planet and the star (1.40).

$$C_{\lambda,\nu} = \frac{\dot{N}^P_{\lambda,\nu}}{\dot{N}^*_{\lambda,\nu}}. \tag{1.40}$$

The low contrast values limit how small and close to the star it is possible to direct image with current technology. With coronography the ratio is increased obscuring the central star. The same principle is present when there is a total eclipse of the Sun. As the moon completely covers the solar disk, it is possible to observe prominences that have much lower brightness than the solar disk.

For an observer, the measured reflected brightness changes the orbital position and surface or atmospheric properties. It is possible to define the phase angle α as the angle between the observer, star and planet along the orbit. If $\alpha = 0$ there is an alignment and the planet is behind the star, at $\alpha = \frac{\pi}{2}$ the planet is seen at its maximum elongation. The characterization of the reflective properties of the surface are expressed by the geometric albedo,A_g:

$$A_g = \frac{F_P}{F_*}\left(\frac{a}{R_P}\right)^2, \tag{1.41}$$

where F_P and F_* are the observed fluxes of the planet and star, respectively. If the thermal emission (self-luminosity) of the planet is relevant it can be corrected by subtracting that contribution from the total observed albedo, A_{obs}. Assuming a planet emitting as a black body:

$$A_g = A_{obs} - \frac{\pi \int_{\lambda_i}^{\lambda_f} I_\lambda(T_{eq}) d\lambda}{F}\left(\frac{a}{R_*}\right)^2, \tag{1.42}$$

with I_λ is computed at the equilibrium temperature. The planet contrast is expressed as a function of the albedo, orbital plane angle function ($\phi(\alpha)$) and ratio between the orbital and planetary radius, C_P.

$$C_P = A_g \phi(\alpha)\left(\frac{R_P}{a}\right)^2. \tag{1.43}$$

Models require a definition of light reflection properties in a spherical surface. Using a Lambert sphere, all the incident light at the surface is reflected in equal amounts in all directions. If the observation is made at an angle θ from a given point of the surface, the intensity decreases proportionally to the $cos(\theta)$. It follows that $\phi(\alpha = 0) = 1$ corresponds the planet behind the star and $\phi(\alpha = \pi) = 0$ to the planet in front of the star, Fig.1.9. If we apply the previous equations to Earth, in the visible $C_{vis}^{\oplus} \approx 10^{-10}$.

To characterize a planet in the Infra-Red (IR) it is useful to define the Bond Albedo. This

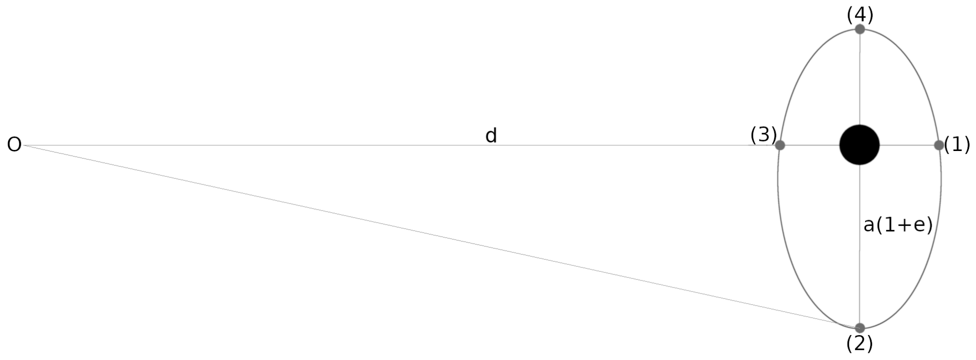

Figure 1.9: An observer at a distance d of a system measures a maximum angular separation θ at maximum elongation $a(1+e)$ if the system is edge-on. The phase angle α varies from 0 if it in front of the star (3) to 1 if it is behind (1). Positions (2) and (4) have the same phase angle, then equal values of α.

quantity expresses the ratio between the emitted and incident bolometric flux. Assuming that the host star emits like a black body, the total luminosity (L) is given by the Stephan-Boltzmann law:

$$L = 4\pi R_*^2 \sigma T_*^4, \tag{1.44}$$

with $\sigma = 5.670 \times 10^{-8}\ Wm^{-2}K^{-4}$, and T_* the effective temperature of the star. At the moment radiation leaves the star, the radiation is distributed in a spherical surface that increases with the distance to the star. For a circular orbit, the incident luminosity on the planet, L_{in}:

$$L_{in} = L\left(\frac{R_*}{a}\right)^2\left(\frac{1-A_{Bond}}{4f}\right). \tag{1.45}$$

The quantity A_{Bond} is the bond albedo and f is a function expresses the redistribution of the energy of the planet caused by its rotation. If the planet is tidally locked only half the planet is irradiated $f = 0.5$; if it is a rapid rotator all the surface is irradiated when integrated in time and $f = 1$. The equilibrium temperature is the expected temperature for a planet that had time to cool down since its formation. If the only contribution is the radiation from the star:

$$T_{eq} = \left(\frac{1 - A_{Bond}}{4f}\right)^{\frac{1}{4}} \left(\frac{R_*}{a}\right)^{\frac{1}{2}} T_*. \tag{1.46}$$

For the Earth $T_{eq} = 254K$, which differs from the mean temperature measured at the surface. This is consequence of the presence of greenhouse gases in the atmosphere. Finally, assuming both planet and star as perfect radiating bodies:

$$C_{IR}(\lambda) = \frac{I_\lambda(T^P_{eq})R^2_P}{I_\lambda(T_*)R^2_*}. \tag{1.47}$$

For the Earth $C^{\oplus}_{IR} = 8.2 \times 10^{-8}$. The direct imaging, when technically possible, gives information about the planet atmosphere structure when combined with wavelength filters. This is a valuable tool, in conjunction with spectroscopy, to detect chemical signatures and possibly bio-markers.

1.4 Characterization of exoplanets atmospheres

The first detection both from absorption features of a transiting exoplanet (Charbonneau et al., 2002) and thermal emission (Charbonneau, 2005) made the debut of the following planetary atmospheres detection and characterization. Detect and characterize exoplanetary atmospheres requires state of the art instruments, high signal-to-noise ratios and dedicated instruments.

1.4.1 Transmission spectroscopy

In an appropriate geometrical configuration, 1.3.2, if a planet crosses the host star disk and its atmosphere will filter the background radiation. The observed transmission spectra will be modulated by its composition, and it will have a different opacity dependence with wavelength. The observed variation of the planet radius as function of wavelength allows the reconstruction of the transmission spectra (Charbonneau et al., 2002).

Lets consider an ideal exoplanet atmosphere in hydrostatic equilibrium. Pressure (P), density

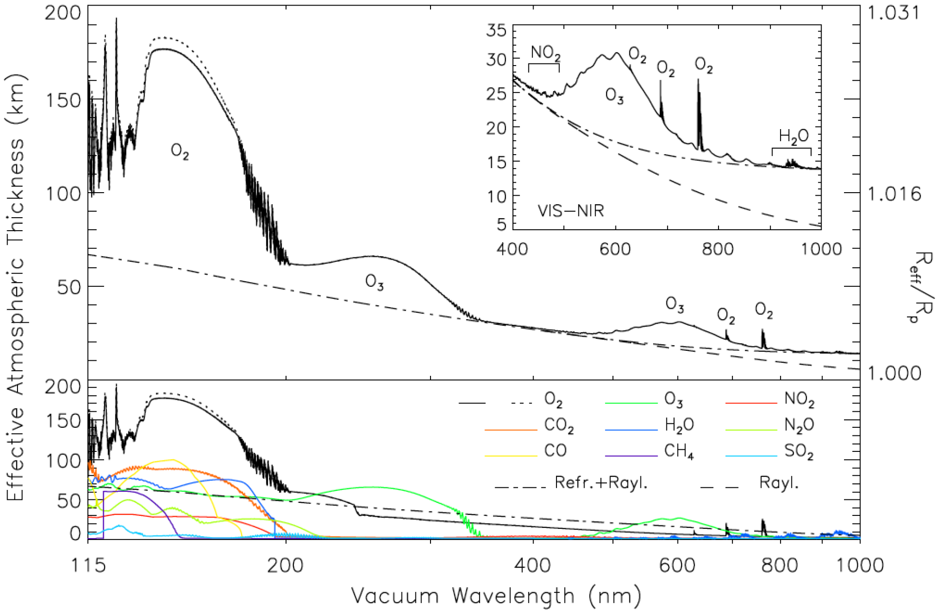

Figure 1.10: Modeled absorption spectra of Earth's atmosphere, covering a spectral range from 1150 to 10000 Å . The presence of molecular oxygen ,ozone, water between others have characteristic response curves with the wavelength. Betremieux and Kaltenegger (2013)

(ρ) and gravity (g) are constant with time. The pressure exerted by a layer in the subsequent one, depends on its surface area and weight. In parallel layers configuration, the equilibrium is expressed by:

$$\frac{dP}{dz} = -\rho g. \tag{1.48}$$

Approximating the layers composition by an ideal gas with mean density ρ, its variation with height is recovered for a slab of temperature T and mean molecular mass m:

$$\rho \propto e^{\frac{-zgm}{k_B T}}. \tag{1.49}$$

The mean molecular mass and temperature are not in general constant with the height, but the previous equations expresses an exponential dependence with z. The observed atmospheric opacity, τ_λ, derived in Ehrenreich et al. (2006), can be computed by the sum of the opacities of the species existent in the atmosphere:

$$\tau_{\lambda} = \sum_{x} \tau_{\lambda,x}, \tag{1.50}$$

where $\tau_{\lambda,x}$ corresponds to the opacity wavelength function for the specie x. Along the line of sight, the amount of atmosphere that filters the background stellar radiation changes with the distance to the planetary surface, h. Defining an impact parameter b:

$$\tau_{\lambda,x}(b) = 2\int_{0}^{+\infty} A_{\lambda,x}\rho_x(h)dl, \tag{1.51}$$

integrating for all possible values of altitude. $A_{\lambda,x}$ is the absorption coefficient of specie x for the wavelength λ. Defining the height as $z = h + R_P$ and rewriting the previous integral, from the surface impact parameter b to the boundary of the atmosphere b_{max}:

$$\tau_{\lambda,x}(b) = 2\int_{b}^{b_{max}} A_{\lambda,x}\rho_x(z - R_P)\frac{zdz}{\sqrt{z^2 - b^2}} \tag{1.52}$$

The first identification of a species in an exoplanetary atmosphere was of a sodium doublet at 5890 $\AA$ (Charbonneau et al., 2002); and later potassium in hot Jupiter's (e.g. Sing et al. (2011)). The water molecule is by far the most commonly observed molecule, mostly because of its particular imprint in the spectra (e.g. Swain et al. (2008),Deming et al. (2013) , Fraine et al. (2014)). For an atmosphere where the most significant contribution comes from scattering, the cross section σ dependence with the wavelength follows:

$$\sigma = \sigma_0\left(\frac{\lambda}{\lambda_0}\right)^{\alpha}, \tag{1.53}$$

with $\alpha = -4$ for Rayleigh scattering. Lecavelier Des Etangs et al. (2008) finds an expression that describes the slope of the planet radius with the logarithm of the wavelength and relates it with the temperature:

$$\frac{dR_p}{dln(\lambda)} = \frac{k_B\alpha}{\mu g}T. \tag{1.54}$$

1.4.2 Emission and reflection

Phase Curves

The brightness of a planet changes with its orbital position and albedo, depending of the relative phase measurement. The observed albedo, equation (1.42), is a measure of the reflected portion of the radiation from the star and the self emission of the planet. Phase curves allow the quantification of the ratio between both sources. At IR the major contribution for the planetary source is its self emission, while at blue Rayleigh scattering takes an important role (Madhusudhan et al., 2014). The expected depth of the occultation, δ_{ocul}, at this longer wavelength is, without loss of generality:

$$\delta_{ocul} = \left(\frac{R_P}{R_*}\right)^2 \left(\frac{T_P}{T_*}\right). \tag{1.55}$$

For a old enough planet T_P should express the equilibrium temperature, as defined on section 1.3.3.4. Non-homogeneous reflection or emission can be recovered. It was detected hot spots, for example, in tidally locked hot Jupiter's like $HD189733b$ (Knutson et al., 2007), the chemical composition or presence of clouds (Placek, Angerhausen, and Knuth, 2017) using chromatic curves.

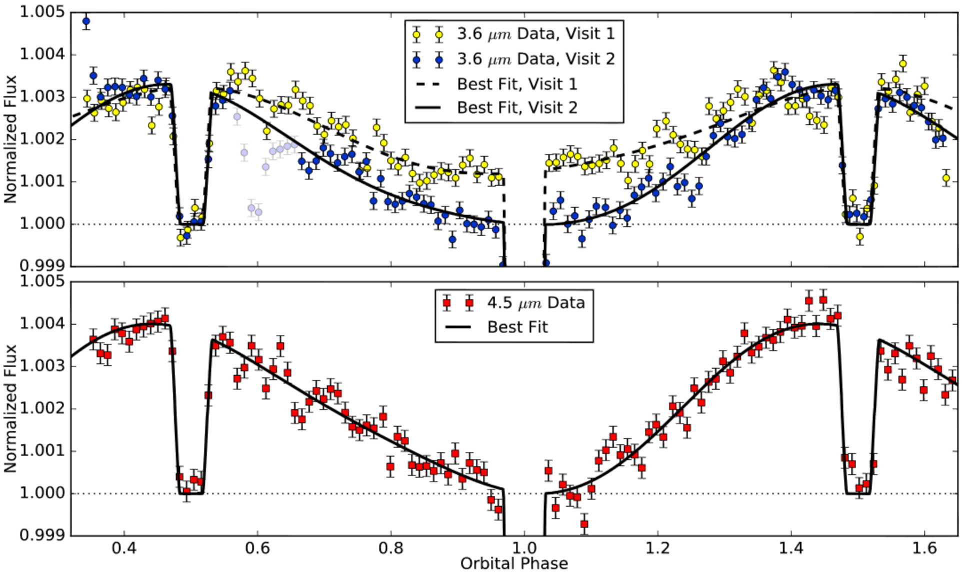

Figure 1.11: Phase curves of $WASP-43b$ at 3.6 and 4.5 μm. The black solid and dashed lines represent the best fit curve, while the dots the observations with the respective error bars. The deep at 1.0 orbital phase corresponds to a transit. The data is normalized by the flux at the time of occultation at phase 0.5 and 1.5 . Credits: Stevenson et al. (2017).

High-dispersion spectroscopy

During the orbital motion around a star, the radial velocity component of the planet in the line of sight of the observer changes. The contrast and angular distance between planet and star are usually not enough to measure directly this effect. The cross-correlation function is used in conjunction with the template of the species being probed. A signal of a species presence is manifested as characteristic velocity phase curve and a maximum of the cross correlation. Assuming the individual lines of molecular bands are not blended in the stellar background spectra, the necessary signal-to-noise ratio to have a detection (Snellen et al., 2015) is, in a first order approximation:

$$\frac{S}{N} = S_P \sqrt{\frac{N_{lines}}{S_* + \sigma^2_{Background} + \sigma^2_{RON} + \sigma^2_{Dark}}}, \tag{1.56}$$

where S_P and S_* are the planetary and stellar signals, $\sigma_{Background}, \sigma_{RON}, \sigma_{Dark}$ are the noise from background, CCD readout and dark current. The detection of a molecular features increases with the multiplicity of line it produces and can be measured simultaneously. The observed albedo of a planet, equation (1.42), main contribution in the optical is from the reflected light.

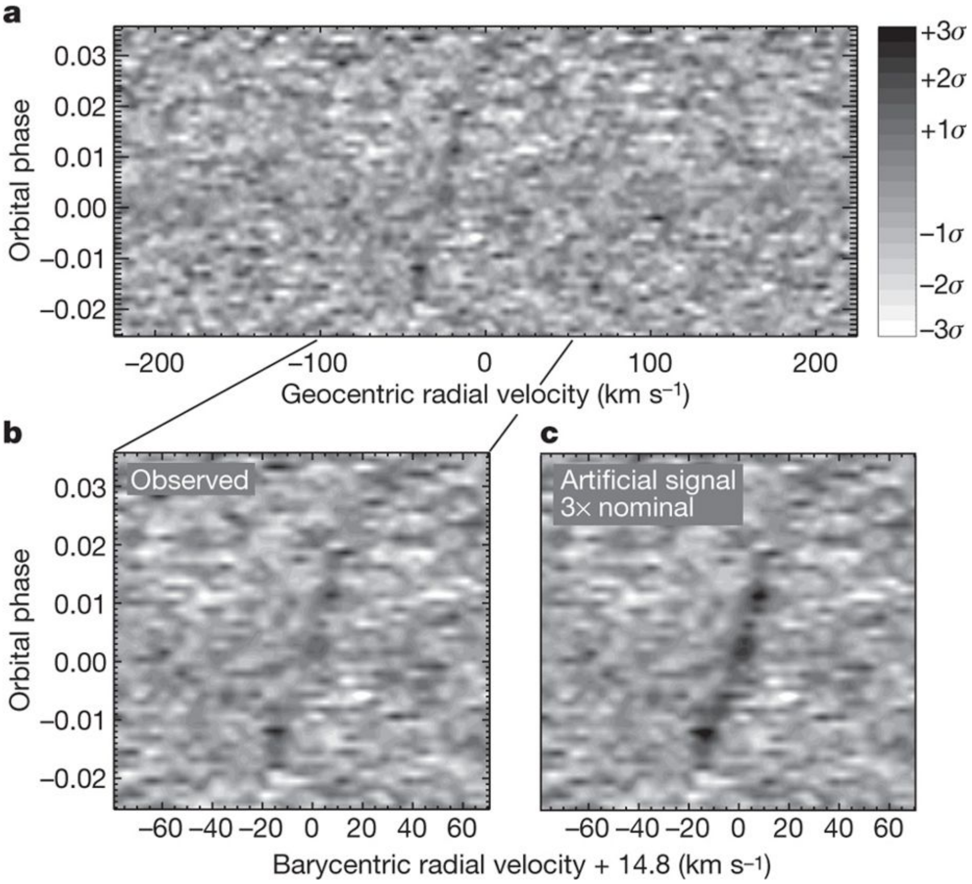

Figure 1.12: Detection of a CO signature for the planet $HD209458$. It is shown the cross-correlation between 56 lines of a CO template and the spectra obtained by the Very Large Telescope. The signal appears with a velocity equal to the sum of the host-star systemic and the observatory relative velocities, $\approx 26Kms^{-1}$. Credits:Brogi et al. (2016)

At this wavelength range the contrast between the planet and star is not optimal for detection, 1.3.3.4. The use of a CCF with a binary mask, makes it possible to construct an average spectral line with an increased signal-to-noise ratio, when compared with single line profiles (Martins et al. (2013)). Using this technique, Martins et al. (2015) was able to detect the reflected light from $51Pegb$, and infer its mass and orbital inclination.

Chapter 2.

Using the Rossiter-McLaughlin effect to characterize atmospheres

The Rossiter-McLaughlin effect, RM, is an apparent anomaly in the measured radial velocity time-series of a star. As a planet transits, the stellar disk behind the planet is blocked. In a rotating star, the fraction of the surface rotating towards the observer has an intrinsic blueshift that is canceled by the radial velocity of the fraction rotating away. A transiting planet creates an unbalance in the total radial velocity that is summed to the proper motion of the star. The fraction and shape of the anomaly depends on the geometry of the system and physical properties, namely but not limited to, stellar spectral type, effective temperature, macroturbulence and radius.

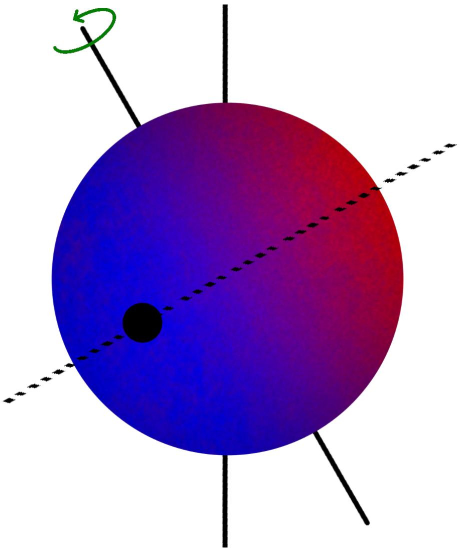

Figure 2.1: Depiction of the Doppler effect due to stellar rotation. As the stellar surface rotates about the axis, the radial component of velocity in the line of sight of the observer is perceived by a change in frequency in the observed light.

2.1 Rossiter-McLaughlin effect

The limb darkening is a radial effect produced by the observation of layers of different temperatures in line of sight. Approaching the stellar limb, the optical thickness increases and the main contribution for the observed flux comes from the cooler top layers. Starting with uniform disk where the limb-darkening contribution can be neglected, the disk is defined by an uniform intensity I_0 defined within the stellar radius. The intensity varies with the position of the planet at each point (x, y) of the surface:

$$I(x,y) = \begin{cases} I_0, & \text{if (x,y)} \in \text{D} \\ 0, & \text{otherwise} \end{cases} \tag{2.1}$$

with the domain D that satisfies the condition: $x^2 + y^2 \leq R_*^2 \wedge (x - x_P)^2 + (y - y_P)^2 \geq R_P^2$; and (x_P, y_P) the center coordinates of the planet. The function $I(x, y)$ changes in time, as the planet orbits around the star. For a full phase, when the disk of the planet is completely inside the stellar disk, the effective allowed values of planet coordinates are:

$$(x_P^2 + y_P^2) \leq (R_* - R_P)^2. \tag{2.2}$$

The integration over the full transit expresses the radial velocity anomaly inside the disk (Ohta, Taruya, and Suto, 2005):

$$\Delta v_* = \Omega_* x_P(t) sin(I_*) \Big(\frac{\gamma^2}{1-\gamma^2}\Big), \qquad \gamma = \frac{R_P}{R_*}, \tag{2.3}$$

where Δv_*, Ω_*, I_* represents the variation in linear velocity, the angular velocity and the inclination of the star. In the discussed conditions, the RM curve is defined mostly by the position of the planet. During ingress and egress the area covered by the occultator changes in time with the planet position. At this moments, the position of the planet satisfies $R_* - R_P < \sqrt{x_P^2 + y_P^2} < R_* + R_P$ and (2.3) is multiplied by a term that expresses the distance between the center coordinates of the planet and the intersection of the planet and the disk. The limb-darkening can be introduced like a correction in the equation (2.3). Adopting a linear model, the intensity of the disk changes with the position of the planet. The intensity function (2.1) is modified in order to compensate this effect, introducing a limb-darkening coefficient, ϵ and a angular parameter that expresses the radial symmetry μ:

$$I(x,y) = \begin{cases} I_0[1-\epsilon(1-\mu)], & \text{if (x,y)} \in \text{D} \\ 0, & \text{otherwise} \end{cases} \tag{2.4}$$

with $\mu = \sqrt{1 - \frac{x^2+y^2}{R_*^2}}$.

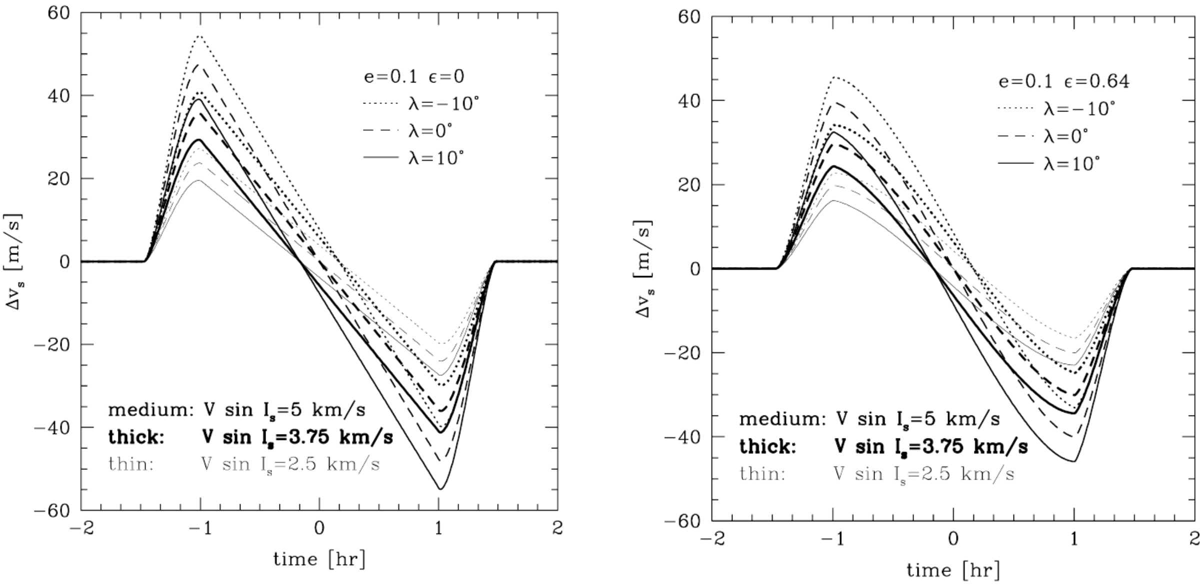

(a)

(b)

Figure 2.2: The Rossiter-McLaughlin anomaly for diverse stellar rotational velocities, $Vsin(i)$, and spin-orbit misalignment values. The planet is assumed to orbit the star with an elliptical orbit with eccentricity of 0.1. In panel 2.2a there is no limb-darkening effect considered. In panel 2.2b it is considered a linear law with coefficient $\epsilon = 0.64$. The main observed effect is a decrease in amplitude and smoothing of the radial velocity curves both at the ingress and egress. Credits: Ohta, Taruya, and Suto (2005).

2.1.1 AROME

The measurement of the Doppler shift of a spectra can be made using two main methods. The iodine cell technique (ICT) fits an observed spectrum A with a reference shifted one A_0 (Butler et al., 1996). The CCF technique uses a cross correlation function between A and A_0 and a Gaussian fit to estimate the radial velocities (Baranne et al., 1996). The work of Boué, G. et al. (2013), which models the RM effect, lead to the implementation of the software $AROME$ for both techniques, deducing also an analytic expression for the velocity using the

CCF technique, from now on $CCFT$. In the line of sight of an observer, the average measured velocity, $\overline{v}$, is proportional to the average velocity of the star surface blocked by the planets, v_P; and the fraction of light blocked in the path f:

$$\overline{v} = \frac{f}{f-1} v_P. \tag{2.5}$$

The previous expression is exact but biased by stellar rotation. Hirano et al. (2009) derived an expression assuming Gaussian line profiles for both rotating and non-rotating stars, departing from the ICT reduction principles . The velocity that maximizes the cross-correlation function is obtained in a similar way the χ^2 of the iodine cell technique fit is minimized.

$$v_{ICT} = -\left(\frac{2\beta_*^2}{\beta_*^2+\beta_P^2}\right)^{\frac{3}{2}} f v_P exp\left(1 - \frac{v_P^2}{2(\beta_*^2+\beta_P^2)}\right), \tag{2.6}$$

where v_P is the planet velocity transiting the disk and β_P, β_* are the Gaussian profiles standard deviations if defined as follows:

$$G_\sigma = \frac{1}{\sqrt{2\pi}\sigma} e^{\frac{-v^2}{2\sigma^2}}; \tag{2.7}$$

corresponding to a normalized Gaussian of dispersion σ.Defining $F_*(v)$,$F_P(v - v_P)$ and $F_{transit}$ as the line profiles of the star, planet with a velocity centered at $v = v_P$ and transit integrated over the stellar surface; it can be constructed a general formulation for the $CCFT$ velocity:

$$v_{CCFT} = \frac{-4\sigma_0\sqrt{\pi}}{a_0} f[(vG_{\sigma_0}) * F_P](v_P), \tag{2.8}$$

which expresses a Gaussian fit of the planetary signal in a first order approximation. The constants a_0 and σ_0 represent the best CCF fit line profile outside transit parameters. Assuming now a more restrictive scenario, where the planet line profile is Gaussian, $F_P = G_{\beta_P}$, the previous equation is written as:

$$v_{CCFT} = -\frac{1}{a_0}\left(\frac{2\sigma_0^2}{\sigma_0^2+\beta_P^2}\right)^{\frac{3}{2}} f v_P exp\left(1 - \frac{v_P^2}{2(\sigma_0^2+\beta_P^2)}\right), \tag{2.9}$$

expression that exactly matches v_{ICT} if $a_0 = 1$ and $\sigma_0 = \beta_*$ corresponds the stellar Gaussian dispersion profile. The planet dispersion parameter β_P has the contribution of the non-rotating line width combined to a correction for the rotational broadening. The perturbation term vanishes in a first order approximation, and the second orders ones express the rotational contribution. The shape of the curves, in special during the ingress and egress, are affected by the limb darkening and second derivatives as result. Furthermore, when entering and leaving the stellar disk, the geometry is not circular and the variation of the area is relevant for the output shape curve.

2.1.2 CARM-ChromAtic Rossiter–Mclaughlin

CARM is an implementation in Python in order to generalize and automate the numerical estimate of the radius of a planet and retrieve the transmission spectra from ground based telescopes. During a transit, the radial velocity variation is imprinted in the stellar spectra. The change depends on the area of planet passing in front of it. If the planet has an important atmosphere, whose composition allows interactions with the background stellar light, there will be a change in the measurement of the planet radius with the wavelength. At visible wavelengths, the main contribution comes from Rayleigh Scattering. Raw spectral data is calibrated and the CCFs extracted by the ESO Pipeline. The CCFs are the numerical result of the cross correlation between the calibrated data and a stellar mask with the approximated target spectral type. The radial velocities are obtained by the sum of the CCFs of each spectral order into a master CCF. The resulting output is adjusted by an unidimensional Gaussian function, in which the extracted radial velocity corresponds to the mean.

The depth and width of each CCF is self-consistent with the expected weight to the output radial velocity. The uncertainty is obtained considering both the photon noise contribution using the calibrated spectra or a similar method using the slope of the resulting CCF. For the chromatic analysis, the CCFs are summed in bins of spectral order, which corresponds directly to wavelength intervals. It is executed a first fit to the white-light to estimate the parameters that are wavelength independent.

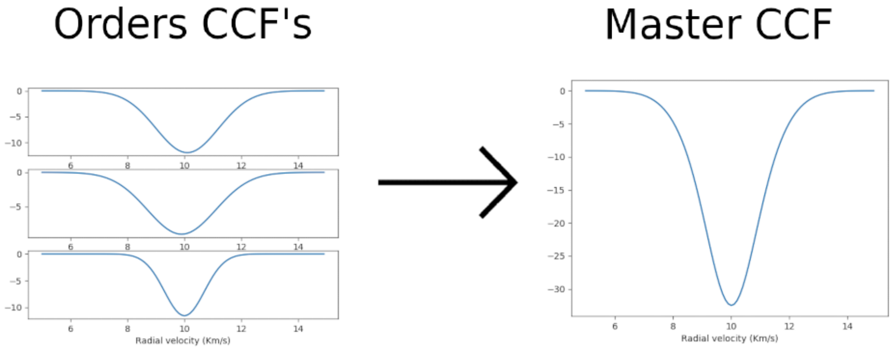

Figure 2.3: CCFs obtained after the ESO pipeline are summed into a master CCF to each wavelength interval. The physical and chemical properties of the atmosphere determine the apparent planetary radius measured by the observer. This method is appropriate when a full direct spectra of the planet cant be directly obtained, giving an estimate of the transmission spectra profile and its temperature.

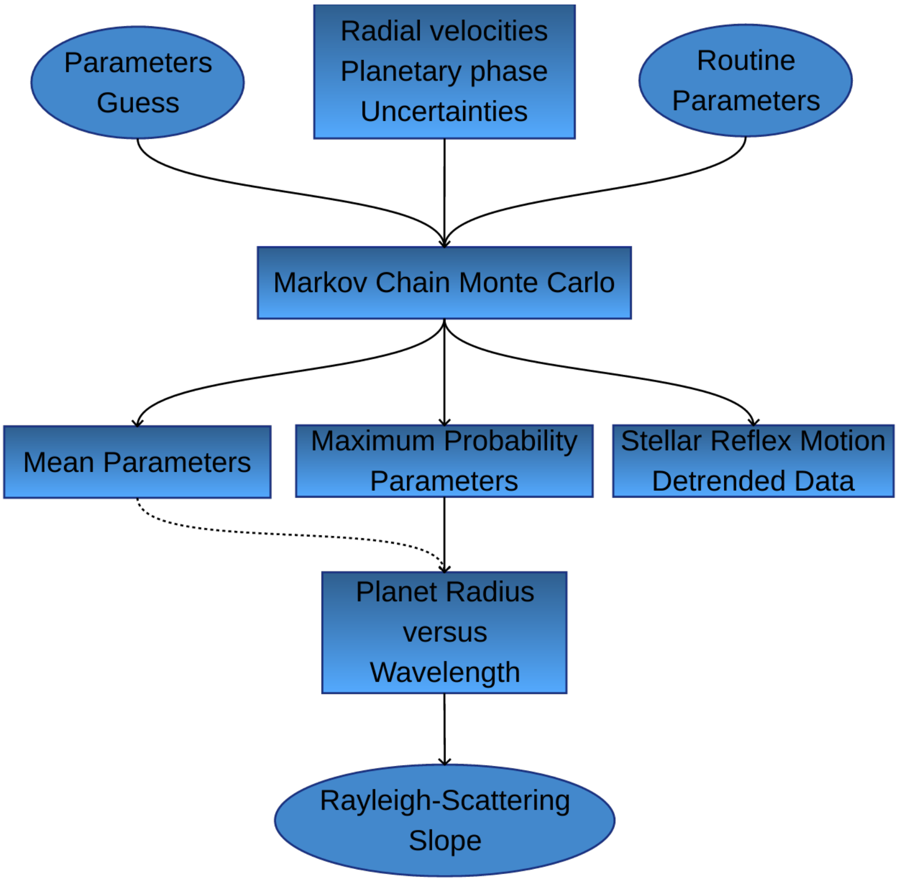

Figure 2.4: The radial velocities obtained by the Gaussian fits, the respective uncertainties and orbital phases jointly with a guess of the parameters, usually obtained from previous works, as well as the number of Monte Carlo steps serve as input for the Markov Chain Monte Carlo Algorithm.

The parameters estimate that best model the input data, taking in account the uncertainties, is found with a Markov Chain Monte Carlo (henceforth $MCMC$) algorithm: *emcee*. As inputs, it is defined both the guess for the model parameters, the priors type and the interval in which they are defined. Lets consider an arbitrary data set $D = [X, Y]$, with $X = [x_1, x_2, ..., x_N]$ and $Y = [y_1, y_2, ..., y_N]$ with uncertainties $\sigma_Y = [\sigma_1, \sigma_2, ..., \sigma_N]$. For a model $f(X, \theta)$, where $\theta = \theta_1, \theta_2, \theta_k$ corresponds to the set of model parameters, the probability of representing the data can be found with Bayes theorem:

$$P(f|D, I) = \frac{P(D|f, I)P(f|I)}{P(D|I)}. \tag{2.10}$$

Given a set of assumptions, represented by I, about the physics of the model; $P(D|f, I)$ represents the posterior probability, $P(f|I)$ the prior probability of the model and $P(D|I)$ is a normalization factor that ensures that the probability density function is normalized to unity. The set of assumptions I define in general the range of values allowed for the set of parameters, evaluated both by physical arguments or values found in previous works. In the context of $MCMC$ the absolute value of the probability is not needed, the normalization factor is the same for any given set. The previous equation can be expanded to a more useful form:

$$P(f|D, I) \propto P(D|f, I) \prod_{i=1}^{k} P(D|\theta_i). \tag{2.11}$$

The prior probability of each parameter can be both informative or not. If an estimate of the value $\theta_i = \theta^{'} \pm \Delta\theta^{'}$ is known, a useful probability distribution in a unidimensional Gaussian $G(\theta^{'}, \alpha\Delta\theta^{'})$, where α is a constant that constrains the width of the probability distribution. Otherwise it can be used a Uniform or Jeffrey's prior in the range allowed by the set of model assumptions. If it is supposed a value y_i has a Gaussian error source with standard deviation σ_N, the posterior probability can be approximated by:

$$P(y_i|f, I) = \frac{1}{\sqrt{2}\sigma_i} exp \frac{-(y_i - f(x_i, \theta))^2}{2\sigma_i^2}. \tag{2.12}$$

For the data set D, $P(D|f, I)$ corresponds to the product of the individual data points. The probability for a large number of elements in D is a very small value. To overcome potential numerical errors the probabilities are usually expressed in term of the logarithm:

$$log(P(D|f, I)) \propto - \sum_{i=1}^{N} \frac{(y_i - f(x_i, \theta))^2}{s_i^2} + ln(2\pi s_i^2), \tag{2.13}$$

where $s_i^2 = \sigma_i^2 + \sigma_w^2$ is the standard deviation of each y_i data point underestimated by a fraction of the model, white noise related $sigma_w$. The Uniform and Gaussian priors can be written as:

$$ln(U(x, x_i, x_f)) = \begin{cases} 0, & \text{if x} \in [x_i, x_f] \\ -\infty, & \text{otherwise} \end{cases} \tag{2.14}$$

$$ln(G(x, \mu, \sigma)) = -\frac{(x-\mu)^2}{2\sigma^2} - \frac{1}{2}log(2\pi) - 2log(\sigma). \tag{2.15}$$

The *MCMC* algorithm is initialized with a set of chains, constructed with a random Gaussian distribution of values around the unknown parameters. Each chain is evaluated and the value of $log(P(f|D,I))$ is computed in parallel. The Monte-Carlo scheme then allows a given step for each unknown, exploring the phase space of parameters and finding both the set that maximizes the probability and the set that is an average of the posterior distribution of each one. The run of a instance of *CARM* results in a fits file containing the following data and keywords:

- *parmax*: set of parameters that maximize the joint posterior probability distribution of D;
- *chains*: matrix in which each line contains the accepted values of the Monte-Carlo algorithm;
- *meanpar*: set of parameters that average the joint posterior distribution of D;
- *lnprob*: natural logarithm of the likelihood of the chosen model representing that data, same as $P(D|f,I)$;
- *jointdata*: arrays containing the orbital phase, radial velocity and uncertainty of the full data set;
- *samplerchain*: condensed $1D$ arrays containing all the information in *chains*;
- *maxpar*: set of parameters that maximize the joint posterior probability for the joint set of data.

The extraction of the results is made independently with *read.py*. The $White$ and $Chromatic$ analysis are identified by fits keywords in each extension in order to obtain a sequential reading of the output.

Chapter 3.

Results

$HD189733b$ is a well studied planet, it has been observed in photometric transits (Beaulieu et al., 2008), the phase curves were obtained (Knutson et al., 2012), it was detected Rayleigh scattering and signatures of dust combining ground based and Hubble-Spitzer orbital observations (Pont et al., 2013). As a way of validation the $CARM$ algorithm was applied for the same data and similar set of model parameters described in Di Gloria, Snellen, and Albrecht (2015). In this work it is analyzed three in-transit observations acquired using the High Resolution échelle spectrograph mounted on the 3.6m telescope at the ESO observatory of La Silla, in Chile. The three sets were obtained under the program $079.C - 0828$, from which it was used the observation from the nights of 29^{th} August, 20^{th} July 2007 and 8^{th} September 2006. The parameters presented on table 3.1 were fixed and the ones on the 3.2 were let free.

Parameter	Value	Units	Source
a	0.03120	A.U.	Triaud et al. (2009)
R_*	0.766	$R_\odot$	Triaud et al. (2009)
i	85.508	Degrees	Triaud et al. (2009)
λ	-0.85	Degrees	Triaud et al. (2009)
$V sin(i)$	3.10	$Km\,s^{-1}$	Triaud et al. (2009)
β_0	1.3	$Km\,s^{-1}$	Di Gloria, Snellen, and Albrecht (2015)
σ_0	3.3	$Km\,s^{-1}$	Di Gloria, Snellen, and Albrecht (2015)
z	4.0	$Km\,s^{-1}$	Di Gloria, Snellen, and Albrecht (2015)
P	2.218573	Days	Triaud et al. (2009)

Table 3.1: Parameters set as known, therefore fixed, for the model used by $CARM$: the Rossiter-McLaughlin effect reproduced by $AROME$ and a Keplerian to represent the reflex motion around the center of mass. The semi-major axis is represented by a, in a approximated circular orbit, R_* the host star radius, i the inclination, λ the spin-orbit misalignment, $V sin(i)$ the rotational velocity of the star projected in the observation line of sight, β_0 the CCF standard deviation for a non-rotating star, σ_0, z and P the orbital period.

Parameter	Guess	Prior Type	Prior parameters	Units
V_i	-1.8	Uniform	$U_i = -1.08$, $U_f = 2.52$	$Km\,s^{-1}$
R_P	0.1585	Gaussian	$\mu = 0.1585$, $\sigma = 0.03$	R_*
K	0.20	Uniform	$U_i = 0.0$, $U_f = 0.4$	$Km\,s^{-1}$
$log(\sigma_W)$	-16	Uniform	$U_i = -16$, $U_f = -1$	$---$

Table 3.2: Parameters set as variable for each data set. The reflex motion velocity V_i is fitted independently for each night. The planet radius, the Keplerian amplitude and white noise parameters are common variables.

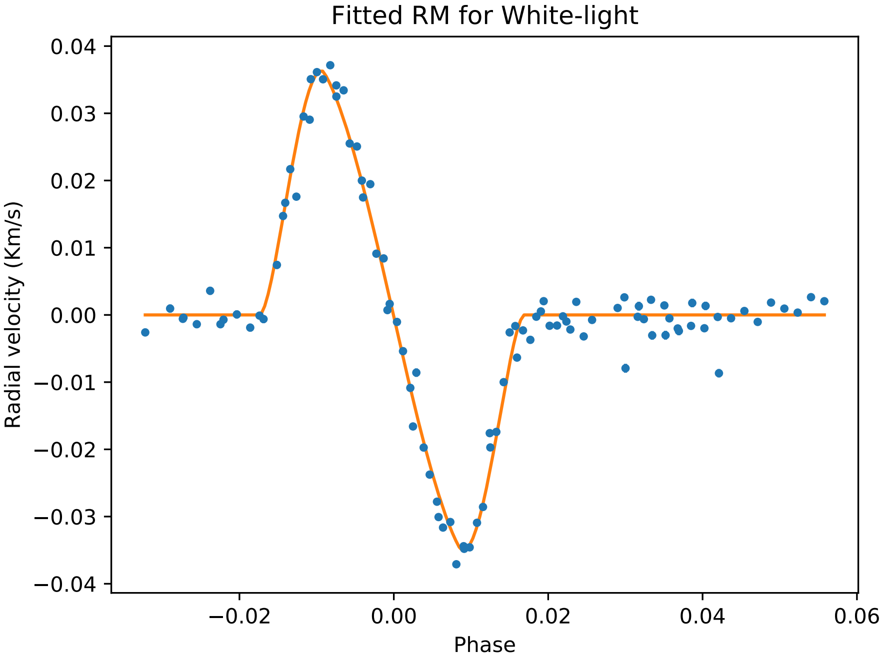

Figure 3.1: Fit that maximizes the probability for the joint data for all orders and nights. From the original data it was subtracted the Keplerian contribution for each set, resulting uniquely on the Rossiter-McLaughlin velocity anomaly.

In particular the reflex motion of the star around the star-planet barycenter is removed independently to each night, as it is calibration and time dependent. The amplitude and planet radius are assumed wavelength dependent, the same for each observation campaign, and let free to adjust the RM effect. The cross correlation functions for each night where obtained using a $K0$ spectral template, matching closely the spectral type of the star. For the white-light the radial velocity obtained, after the data was combined, presents a distinct and well defined RM anomaly, Fig.3.1.

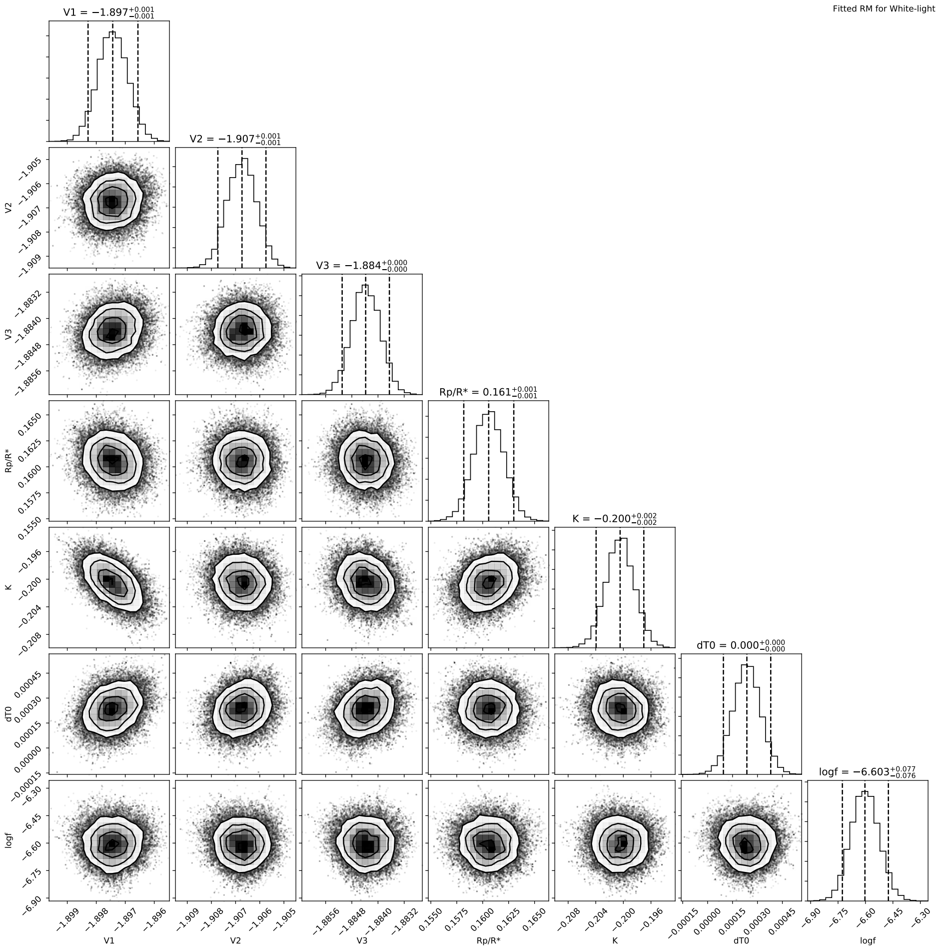

Figure 3.2: White-light corner plot obtained from the sum of the CCFs for each order (equivalent to the last order of HARPS). The values estimated for the parameters have ≈ 68% confidence interval around the mean. $V1$, $V2$ and $V3$ expresses the velocity shift around the center of mass of the system for the different data sets, $dT0$ the shift of mid-transit phase accounting for errors in the period determination and $logf$ the uncorrelated white noise contribution for the data.

To estimate the parameters that best fit the data, the limb darkening coefficients where estimated for both white light and chromatic bins with the *LDTK* package (Parviainen and Aigrain, 2015). It is obtained a radius estimate of $R_P/R_* = 0.161 \pm 0.003$, in line with the results obtained by Pont et al. (2013) and Di Gloria, Snellen, and Albrecht (2015). The spectral response is obtained, as described in chapter 4, fitting the chosen wavelength bins and obtaining the estimated radius. In Fig.3.3 the fits are presented at left after the reflex motion subtraction and at right the correspondent residuals.

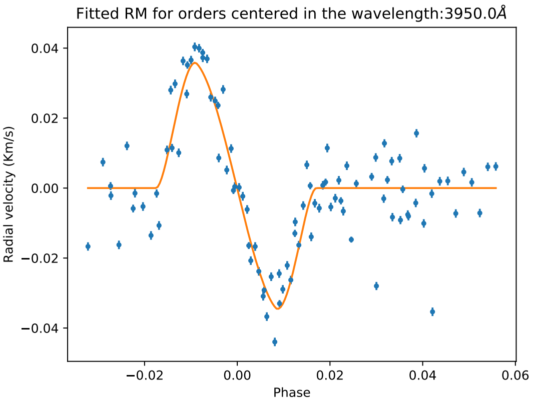
Fitted RM for orders centered in the wavelength:3950.0Å

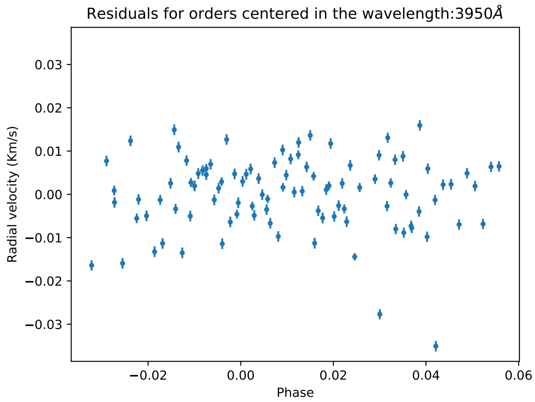
Residuals for orders centered in the wavelength:3950Å

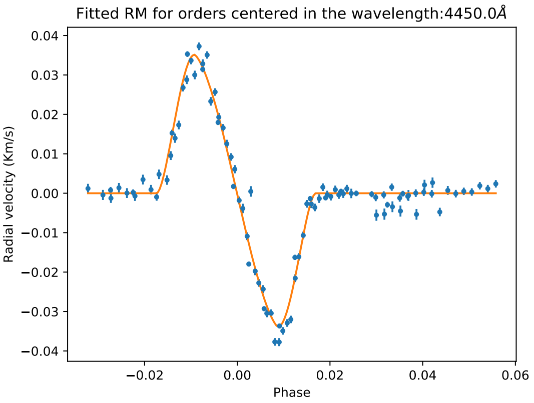
Fitted RM for orders centered in the wavelength:4450.0Å

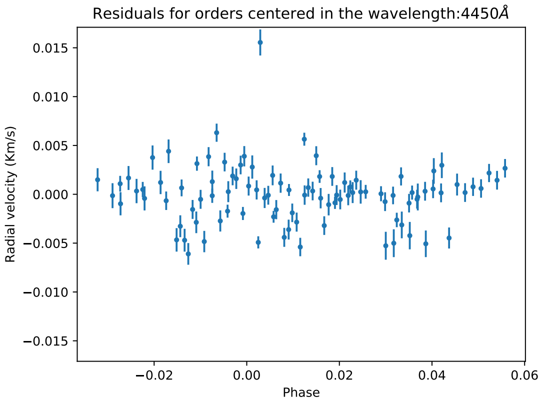
Residuals for orders centered in the wavelength:4450Å

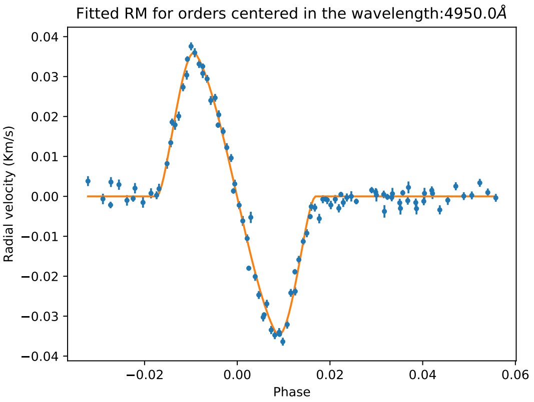
Fitted RM for orders centered in the wavelength:4950.0Å

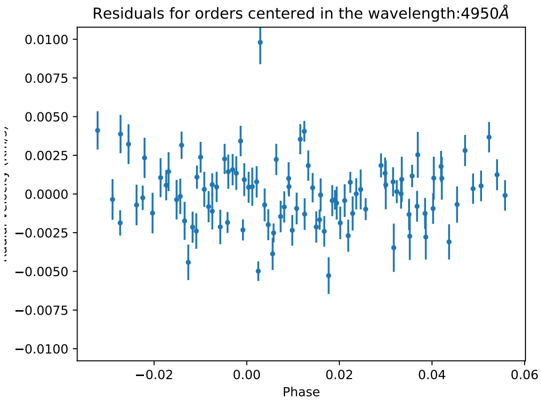
Residuals for orders centered in the wavelength:4950Å

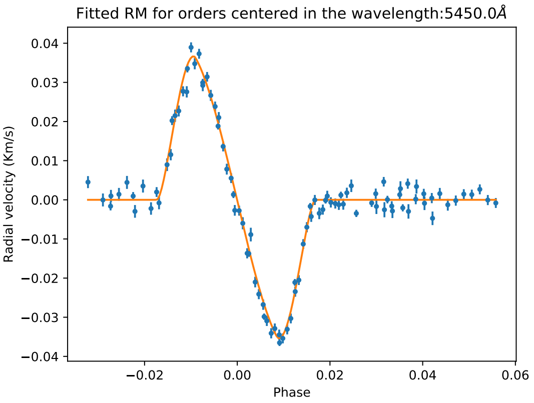
Fitted RM for orders centered in the wavelength:5450.0Å

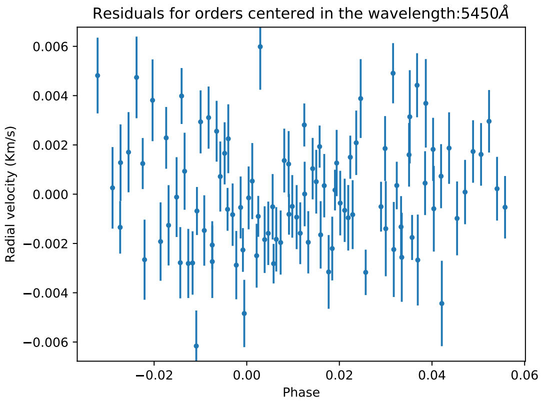
Residuals for orders centered in the wavelength:5450Å

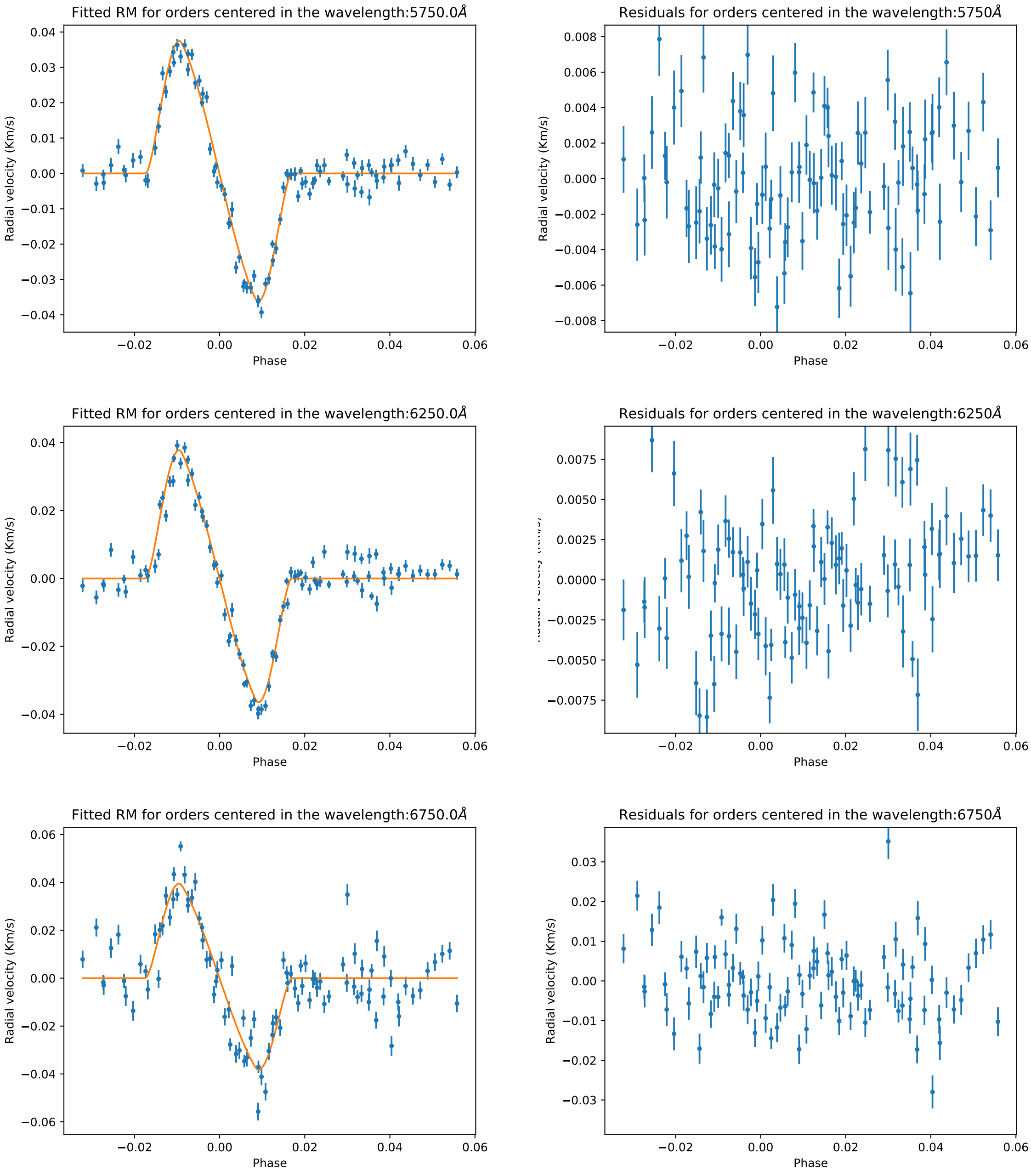

Figure 3.3: Fitted joint data after the removal of the reflex motion with the set of parameters that maximize the probability for the different chromatic wavelength bins. The residuals are obtained after the subtraction of the Rossiter-McLaughlin effect.

When compared with Di Gloria, Snellen, and Albrecht (2015), the residuals are less prone to present visible structure, at least relevant when compared with the error bars. This can indicate, in principle, the method adopted here fits better the observed data. The results can have at least two explanations: the effect subtraction is better because the template mask closely matches the spectral type of the star and/or the simultaneous fitting of the parameters yields a result with a higher confidence level.

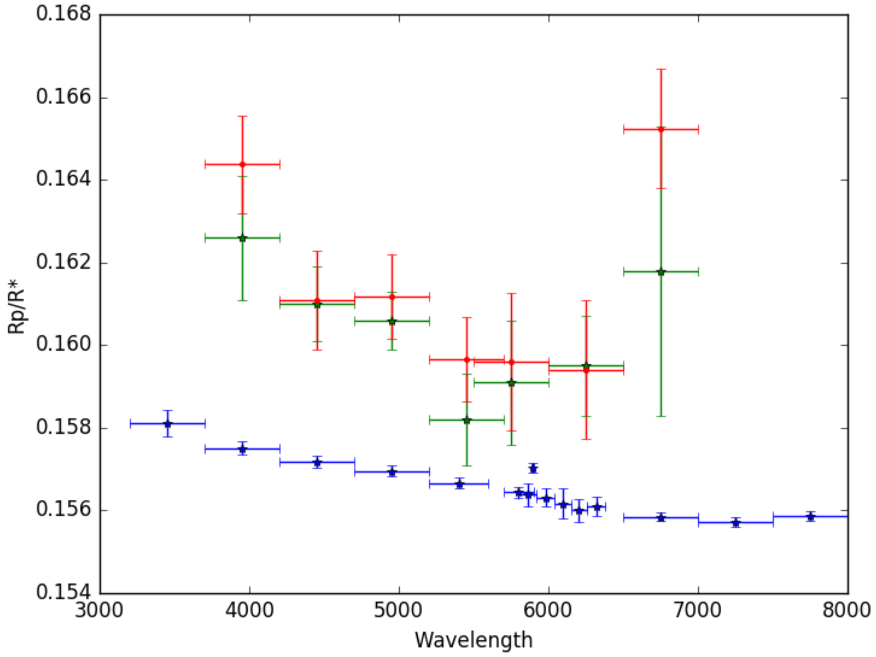

Figure 3.4: Comparison of the radii obtained with this code (blue) compared with the distribution obtained by Di Gloria, Snellen, and Albrecht (2015) using a similar procedure and STIS Pont et al. (2013) transmission spectra in similar wavelength bins.

The obtained slope the transmission spectra closely matches the results obtained before within a 2σ confidence level. Employing expression (1.54), it is found a mean temperature of $2650 \pm 1400K$, agreeing again with the two sources cited before.

Chapter 4.

Conclusions

The Chromatic Rossiter-McLaughlin method was implemented and automated, resulting in *CARM*. The algorithm was applied to HARPS in-transit archival data and the transmission spectrum of HD189733b was retrieved. The procedure was validated comparing to both Di Gloria, Snellen, and Albrecht (2015), whose procedure was replicated with adaptations in this work, and the resulting transmission spectrum from space based observatories (Pont et al., 2013). The radius ratio wavelength relation is highly correlated to the width of the non-rotating star and the projected velocity, $V sin(i)$. Radial velocity alone is insufficient to constrain both parameters, and therefore obtain precise ratios from the curves. A combination of RV and transit photometry has proved to be useful to constrain in a Bayesian fashion different system parameters, increasing furthermore the uncertainty in their determination (Triaud et al., 2009). The slope otherwise is conserved, resulting on a temperature estimate of $2650 \pm 1400K$, in line with the results of Di Gloria, Snellen, and Albrecht (2015). This technique can prove to be of special importance when combined with higher resolution spectrographs like ESPRESSO. With the increased signal-to-noise ratio, the division of the wavelength intervals can be made smaller conserving uncertainties comparable to the ones obtained in this work. On another hand, with the same intervals, the uncertainty on the radius will be smaller and the slope will be better determined, resulting on a better estimate of the temperature. With more precise data, the temperature/pressure profile with the atmosphere height can possibly be recovered. Moreover it will be possible to precisely measure the effect on fainter objects, increasing the number of atmospheres detected and characterized. Such work will be crucial to constrain the number of hypothesis of planetary formation and the nature of the relation of star-planet interactions along their development.

Bibliography

A. Smith, B. and R. J. Terrile (Jan. 1985). “A Circumstellar Disk Around β Pictoris”. In: *Science (New York, N.Y.)* 226, pp. 1421–4. DOI: 10.1126/science.226.4681.1421.

Baranne, A. et al. (Oct. 1996). “ELODIE: A spectrograph for accurate radial velocity measurements.” In: *aaps* 119, pp. 373–390.

Beaulieu, J. P. et al. (Apr. 2008). “Primary Transit of the Planet HD 189733b at 3.6 and 5.8 μm”. In: *The Astrophysical Journal* 677, pp. 1343–1347. DOI: 10.1086/527045. arXiv: 0711.2142.

Beaulieu, J.-P. et al. (Feb. 2006). “Discovery of a Cool Planet of 5.5 Earth Masses Through Gravitational Microlensing”. In: *Nature* 439, pp. 437–40. DOI: 10.1038/nature04441.

Betremieux, Y and L. Kaltenegger (July 2013). “Transmission spectrum of Earth as a transiting exoplanet - from the ultraviolet to the near-infrared”. In: *The Astrophysical Journal Letters* 772. DOI: 10.1088/2041-8205/772/2/L31.

Bouchy, F., F. Pepe, and D. Queloz (2001). “Fundamental photon noise limit to radial velocity measurements”. In: *Astronomy & Astrophysics* 374, pp. 733–739. DOI: 10.1051/0004-6361:20010730.

Boué, G. et al. (2013). “New analytical expressions of the Rossiter-McLaughlin effect adapted to different observation techniques”. In: *A&A* 550, A53. DOI: 10.1051/0004-6361/201220146. URL: https://doi.org/10.1051/0004-6361/201220146.

Brogi, M. et al. (2016). “Rotation and Winds of Exoplanet HD 189733 b Measured with High-dispersion Transmission Spectroscopy”. In: *The Astrophysical Journal* 817(2), 106, p. 106. DOI: 10.3847/0004-637X/817/2/106. arXiv: 1512.05175 [astro-ph.EP].

Burrows, A. S. (2014). “Highlights in the study of exoplanet atmospheres”. In: *nat* 513(7518), pp. 345–352. DOI: 10.1038/nature13782. arXiv: 1409.7320 [astro-ph.EP].

Butler, R. P. et al. (1996). “Attaining Doppler Precision of 3 M s-1”. In: *pasp* 108, p. 500. DOI: 10.1086/133755.

Charbonneau, D. et al. (Mar. 2002). “Detection of an Extrasolar Planet Atmosphere”. In: *The Astrophysical Journal* 568, pp. 377–384. DOI: 10.1086/338770. eprint: astro-ph/0111544.

Charbonneau, D. et al. (2000). “Detection of Planetary Transits Across a Sun-like Star”. In: *The Astrophysical Journal* 529(1), pp. L45–L48. DOI: 10.1086/312457. arXiv: astro-ph/9911436 [astro-ph].

Charbonneau, D. et al. (2005). “Detection of thermal emission from an extrasolar planet”. In: *Astrophys. J.* 626, pp. 523–529. DOI: 10.1086/429991. arXiv: astro-ph/0503457 [astro-ph].

Connes, P. (Mar. 1985). “Absolute astronomical accelerometry”. In: *APSS* 110, pp. 211–255. DOI: 10.1007/BF00653671.

Deming, D. et al. (2013). “Infrared Transmission Spectroscopy of the Exoplanets HD 209458b and XO-1b Using the Wide Field Camera-3 on the Hubble Space Telescope”. In: *The Astrophysical Journal* 774(2), 95, p. 95. DOI: 10.1088/0004-637X/774/2/95. arXiv: 1302.1141 [astro-ph.EP].

Di Gloria, E., I. A. G. Snellen, and S. Albrecht (Aug. 2015). “Using the chromatic Rossiter-McLaughlin effect to probe the broadband signature in the optical transmission spectrum of HD 189733b”. In: *Astronomy & Astrophysics* 580, A84, A84. DOI: 10.1051/0004-6361/201526218. arXiv: 1507.08070 [astro-ph.EP].

Ehrenreich, D. et al. (2006). “The transmission spectrum of earth-size transiting planets”. In: *Astron. Astrophys.* 448, p. 379. DOI: 10.1051/0004-6361:20053861. arXiv: astro-ph/0510215 [astro-ph].

Fischer, D. A. et al. (June 2016). “State of the Field: Extreme Precision Radial Velocities”. In: *Publications of the Astronomical Society of the Pacific* 128(6), p. 066001. DOI: 10.1088/1538-3873/128/964/066001. arXiv: 1602.07939 [astro-ph.IM].

Fraine, J. et al. (2014). “Water vapour absorption in the clear atmosphere of a Neptune-sized exoplanet”. In: *Nature* 513(7519), pp. 526–529. DOI: 10.1038/nature13785. arXiv: 1409.8349 [astro-ph.EP].

Hirano, T. et al. (Oct. 13, 2009). “Analytic Description of the Rossiter-McLaughlin Effect for Transiting Exoplanets: Cross-Correlation Method and Comparison with Simulated Data”. In: *Astrophys.J.709:458-469,2010*. DOI: 10.1088/0004-637X/709/1/458. arXiv: 0910.2365v2 [astro-ph.EP].

Kippenhahn, R. and A. Weigert (1990). *Stellar Structure and Evolution*. Springer, p. 192.

Knutson, H. A. et al. (July 2012). “3.6 and 4.5 μm Phase Curves and Evidence for Non-equilibrium Chemistry in the Atmosphere of Extrasolar Planet HD 189733b”. In: *The Astrophysical Journal* 754, 22, p. 22. DOI: 10.1088/0004-637X/754/1/22. arXiv: 1206.6887 [astro-ph.EP].

Knutson, H. A. et al. (2007). “A map of the day-night contrast of the extrasolar planet HD 189733b”. In: *Nature* 447(7141), pp. 183–186. DOI: 10.1038/nature05782. arXiv: 0705.0993 [astro-ph].

Koch, D. G. et al. (2010). “Kepler Mission Design, Realized Photometric Performance, and Early Science”. In: *The Astrophysical Journal* 713(2), pp. L79–L86. DOI: 10.1088/2041-8205/713/2/L79. arXiv: 1001.0268 [astro-ph.EP].

Konacki, M. and A. Wolszczan (May 2003). “Masses and Orbital Inclinations of Planets in the PSR B1257+12 System”. In: *The Astrophysical Journal* 591. DOI: 10.1086/377093.

Lecavelier Des Etangs, A. et al. (2008). “Rayleigh scattering in the transit spectrum of HD 189733b”. In: *Astronomy & Astrophysics* 481(2), pp. L83–L86. DOI: 10.1051/0004-6361:200809388. arXiv: 0802.3228 [astro-ph].

Leger, A et al. (Aug. 2009). “Transiting exoplanets from the CoRoT space mission”. In: *http://dx.doi.org/10.1051/0004-6361/200911933*.

Lindegren, L. and D. Dravins (2003). “The fundamental definition of ”radial velocity””. In: *Astronomy & Astrophysics* 401, pp. 1185–1201. DOI: 10.1051/0004-6361:20030181. arXiv: astro-ph/0302522 [astro-ph].

Madhusudhan, N. et al. (2014). “Exoplanetary Atmospheres”. In: *Protostars and Planets VI*. Ed. by H. Beuther et al., p. 739. DOI: 10.2458/azu_uapress_9780816531240-ch032. arXiv: 1402.1169 [astro-ph.EP].

Marshall, J. L. et al. (July 2008). “The MagE spectrograph”. In: *Ground-based and Airborne Instrumentation for Astronomy II.* Vol. 7014. procspie, p. 701454. DOI: 10.1117/12.789972. arXiv: 0807.3774.

Martins, J. H. C. et al. (2013). “Spectroscopic direct detection of reflected light from extrasolar planets”. In: *Monthly Notices of the Royal Astronomical Society* 436(2), pp. 1215–1224. DOI: 10.1093/mnras/stt1642. arXiv: 1308.6516 [astro-ph.EP].

Martins, J. H. C. et al. (2015). “Evidence for a spectroscopic direct detection of reflected light from 51 Pegasi b”. In: *Astronomy & Astrophysics* 576, A134, A134. DOI: 10.1051/0004-6361/201425298. arXiv: 1504.05962 [astro-ph.EP].

Mayor, M. and D. Queloz (1995). “A Jupiter - mass companion to a solar - type star.” In: *Nature* 378, p. 355. DOI: 10.1038/378355a0.

Mayor, M et al. (Jan. 2003). “Setting New Standards with HARPS”. In: *The Messenger* 114, p. 20.

Ohta, Y., A. Taruya, and Y. Suto (Apr. 2005). “The Rossiter-McLaughlin Effect and Analytic Radial Velocity Curves for Transiting Extrasolar Planetary Systems”. In: *The Astrophysical Journal* 622, pp. 1118–1135. DOI: 10.1086/428344. eprint: astro-ph/0410499.

Parviainen, H. and S. Aigrain (2015). “LDTK: Limb Darkening Toolkit”. In: *Monthly Notices of the Royal Astronomical Society* 453(4), pp. 3821–3826. DOI: 10.1093/mnras/stv1857. arXiv: 1508.02634 [astro-ph.EP].

Perryman, M. (May 2011). *The Exoplanet Handbook.* Cambridge University Press.

Placek, B., D. Angerhausen, and K. H. Knuth (2017). “Analyzing Exoplanet Phase Curve Information Content: Toward Optimized Observing Strategies”. In: *The Astrophysical Journal* 154(4), 154, p. 154. DOI: 10.3847/1538-3881/aa880d. arXiv: 1708.07589 [astro-ph.IM].

Pont, F. et al. (July 2013). “The prevalence of dust on the exoplanet HD 189733b from Hubble and Spitzer observations”. In: *Monthly Notices of the Royal Astronomical Society* 432, pp. 2917–2944. DOI: 10.1093/mnras/stt651. arXiv: 1210.4163 [astro-ph.EP].

Rupprecht, G et al. (Sept. 2004). “The exoplanet hunter HARPS: performance and first results”. In: *Ground-based Instrumentation for Astronomy. Edited by Alan F. M. Moorwood and Iye Masanori. Proceedings of the SPIE* 5492, p. 148. DOI: 10.1117/12.551267.

Seager, S., R. Dotson, and L. Institute (2010). *Exoplanets*. Space Science Series. University of Arizona Press. ISBN: 9780816529452. URL: https://books.google.pt/books?id=7dV0XyaP2MoC.

Seager, S. and G. Mallén-Ornelas (2003). "On the Unique Solution of Planet and Star Parameters from an Extrasolar Planet Transit Light Curve". In: *Scientific Frontiers in Research on Extrasolar Planets*. Ed. by D. Deming and S. Seager. Vol. 294. Astronomical Society of the Pacific Conference Series, pp. 419–422.

Sing, D. K. et al. (Mar. 2011). "Gran Telescopio Canarias OSIRIS transiting exoplanet atmospheric survey: detection of potassium in XO-2b from narrowband spectrophotometry". In: *Astronomy & Astrophysics* 527, A73, A73. DOI: 10.1051/0004-6361/201015579. arXiv: 1008.4795 [astro-ph.EP].

Snellen, I. et al. (2015). "Combining high-dispersion spectroscopy with high contrast imaging: Probing rocky planets around our nearest neighbors". In: *Astronomy & Astrophysics* 576, A59, A59. DOI: 10.1051/0004-6361/201425018. arXiv: 1503.01136 [astro-ph.EP].

Stevenson, K. B. et al. (2017). "Spitzer Phase Curve Constraints for WASP-43b at 3.6 and 4.5 μm". In: *The Astronomical Journal* 153(2), 68, p. 68. DOI: 10.3847/1538-3881/153/2/68. arXiv: 1608.00056 [astro-ph.EP].

Swain, M. R. et al. (Feb. 2008). "The Mid-Infrared Spectrum of the Transiting Exoplanet HD 209458b". In: *The Astrophysical Journal* 674, pp. 482–497. DOI: 10.1086/523832. eprint: astro-ph/0702593.

Triaud, A. H. M. J. et al. (Oct. 2009). "The Rossiter-McLaughlin effect of CoRoT-3b and HD 189733b". In: *Astronomy & Astrophysics* 506, pp. 377–384. DOI: 10.1051/0004-6361/200911897. arXiv: 0907.2956 [astro-ph.EP].

Wheatley, P. J. et al. (2018). "The Next Generation Transit Survey (NGTS)". In: *Monthly Notices of the Royal Astronomical Society* 475(4), pp. 4476–4493. DOI: 10.1093/mnras/stx2836. arXiv: 1710.11100 [astro-ph.EP].

Wolszczan, A. and D. A. Frail (Jan. 1992). "A planetary system around the millisecond pulsar PSR1257 + 12". In: *Nature* 355, pp. 145–147. DOI: 10.1038/355145a0.

Appendices

Chapter A.

Apendice

As result of the *CARM* routine applied to the archival HARPS data, it was obtained a set of parameters for each wavelength bin. The corner plots for the chromatic intervals can be seen in Fig.A.1 and A.2.

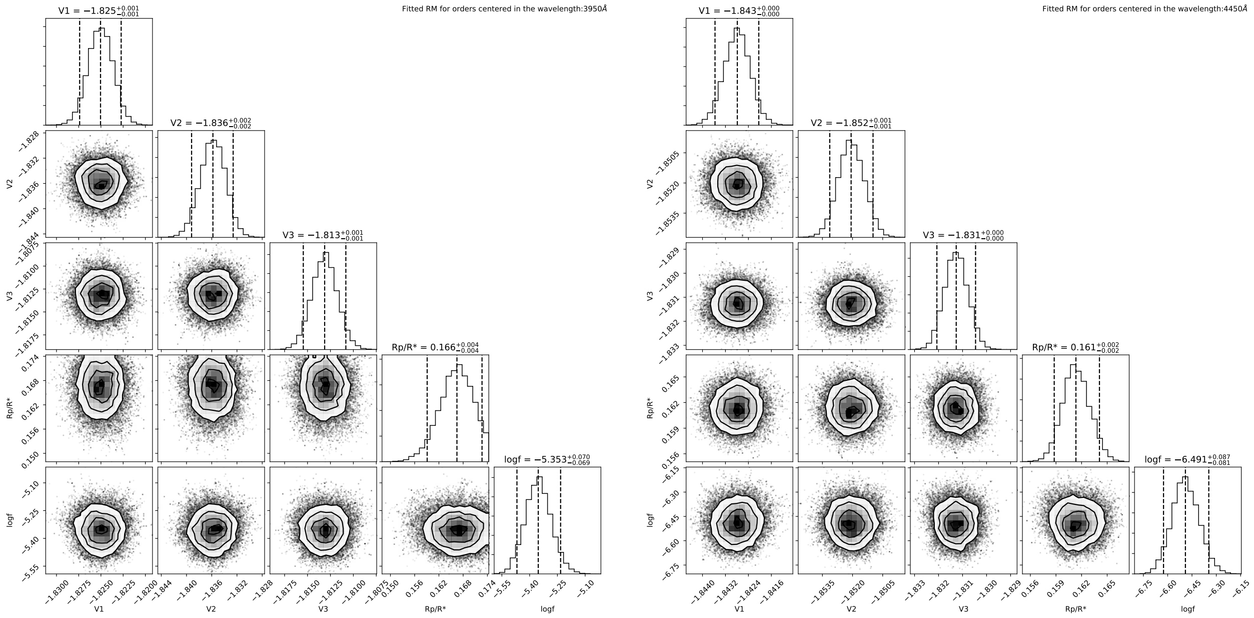

Figure A.1: Corner plots with the joint posterior distribution of the fitted parameters for the wavelengths centered in the 3950$\mathring{A}$ and 4450$\mathring{A}$

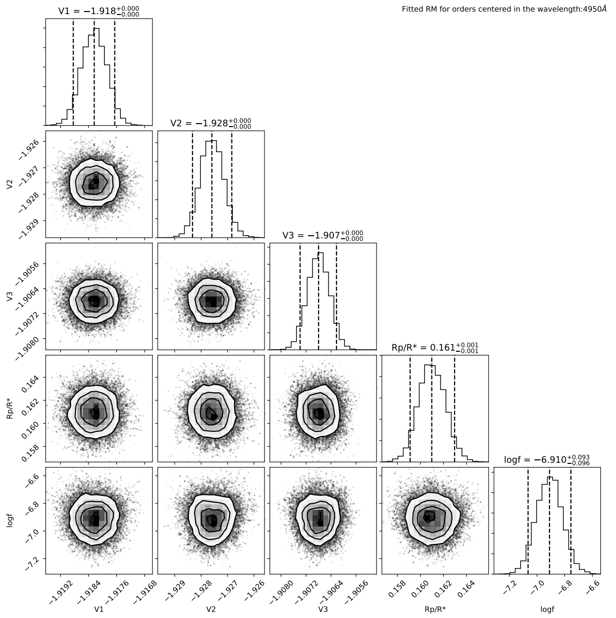

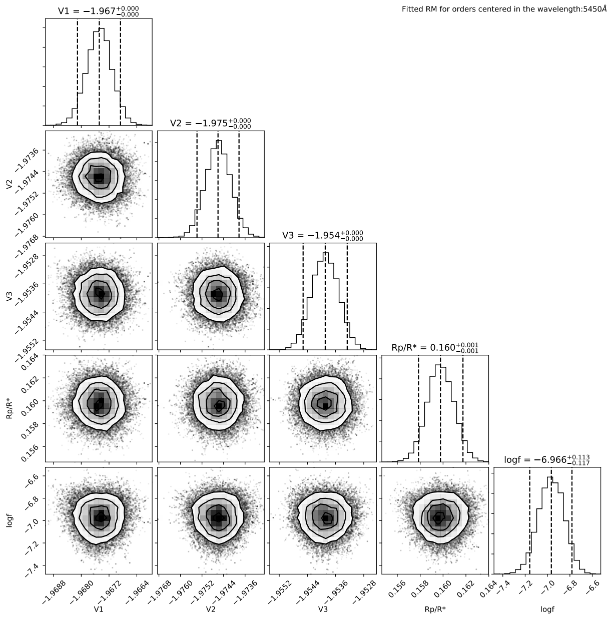

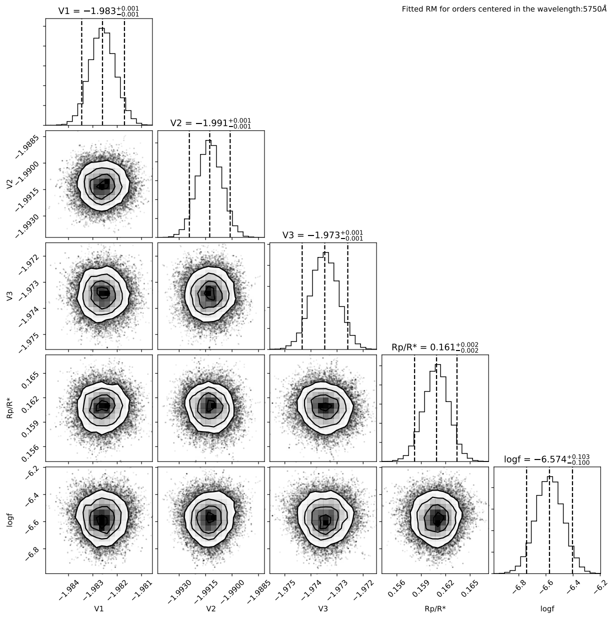

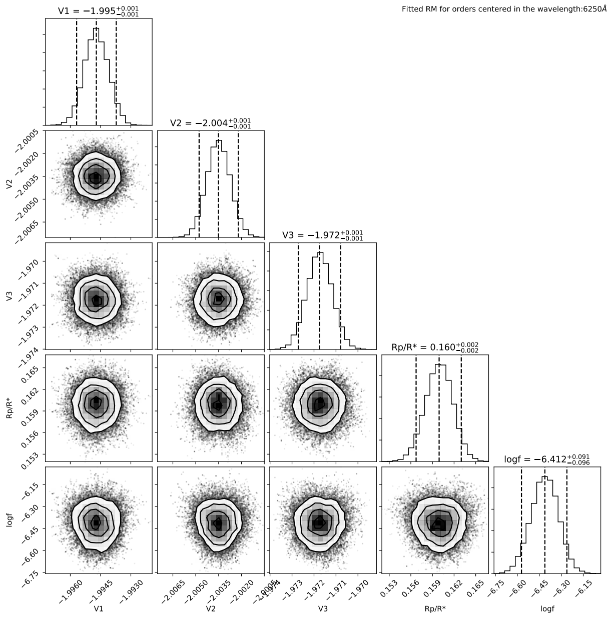

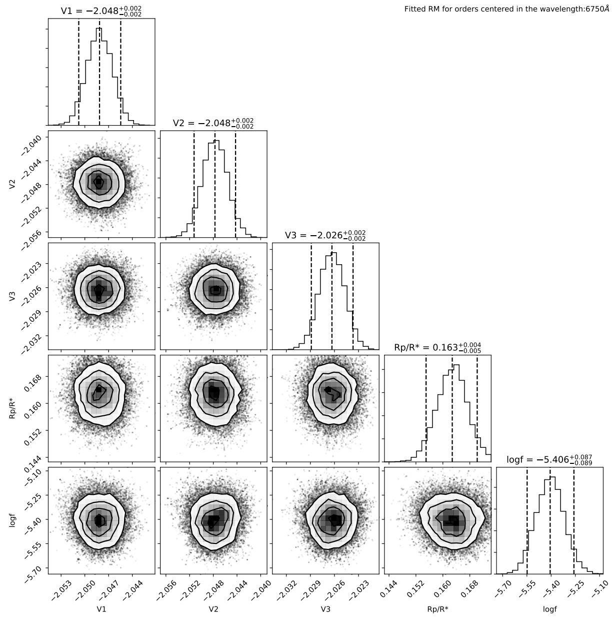

Figure A.2: Continuation of A.1 for the wavelengths 4950Å, 5450Å, 5750Å, 6250Å and 6750Å.